Journal of Palaeogeography, 2026, 15(1): 100295

Available online at www.sciencedirect.com

ScienceDirect

journal homepage: http://www.journals.elsevier.com/journal-of-palaeogeography/

Research article

Palaeoweathering and palaeoclimate of the Lower Cretaceous upper Xiguayuan Formation in the Luanping Basin, North China: Implications for early Aptian global cooling

Long Sun [a,b], *Sheng-He Wu* [a,b,*], *Da-Li Yue* [a,b], *Si-Chong Jiang* [a,b], *Wei Du* [a,b], *Li-Jun Yang* [a,b], *Zhen-Hua Xu* [a,b], *Ke Zhang* [c,d]

[a] *National Key Laboratory of Petroleum Resources and Engineering, China University of Petroleum (Beijing), Beijing 102249, China*
[b] *College of Geosciences, China University of Petroleum (Beijing), Beijing 102249, China*
[c] *China Zhenhua Oil Co. Ltd., Beijing 100031, China*
[d] *Chengdu North Petroleum Exploration and Development Technology Co. Ltd., Chengdu 610051, Sichuan Province, China*

Abstract The Early Cretaceous greenhouse climate was interrupted by multiple intermittent cold snaps such as the Valanginian cold snap and late Aptian climate cooling events, but there is currently a lack of terrestrial palaeoweathering and palaeoclimate records for the early Aptian climate cooling event. The relationship between the regional climate of terrestrial lake basins and the global climate during the early Aptian is still unclear. The Luanping Basin, which is located in the northeastern North China Craton (NCC) and contains Lower Cretaceous sediments with a maximum thickness of ~3200 m, is an ideal place for analysing the terrestrial weathering and climate. Sixteen mudstone samples were collected from the Lower Cretaceous upper Xiguayuan Formation in the Luanping Basin. The mineral compositions and major, trace and rare earth element contents of the mudstone samples were quantitatively determined via X-ray diffraction (XRD), X-ray fluorescence (XRF), and inductively coupled plasma–mass spectrometry (ICP–MS), respectively. Elemental geochemical analyses were carried out to determine palaeoweathering intensity, palaeoclimatic conditions, and their relationships with the global climate. The variation trends in multiple chemical weathering indices are reconstructed after the interference of nonweathering factors is eliminated, reflecting that the source area has experienced mainly weak to moderate weathering. After evaluating the influences of carbonate-sourced elements, we infer that the regional palaeoclimate is arid and cold on the basis of the Sr/Cu ratio, Rb/Sr ratio, C-value, land surface temperature (LST), and mean annual temperature (MAT). All chemical weathering indices and palaeoclimate proxies exhibit similar trends. Moreover, the cooling of palaeotemperatures could have been a response to the early Aptian global cold snap. The regional climate of

* Corresponding author. National Key Laboratory of Petroleum Resources and Engineering, China University of Petroleum (Beijing), Beijing 102249, China.
E-mail address: reser@cup.edu.cn (S.-H. Wu).
Peer review under responsibility of China University of Petroleum (Beijing).
https://doi.org/10.1016/j.jop.2025.100295
2095-3836/© 2025 The Author(s). Published by Elsevier B.V. on behalf of China University of Petroleum (Beijing). This is an open access article under the CC BY license (http://creativecommons.org/licenses/by/4.0/).

the Luanping Basin is controlled mainly by global climate change, which provides terrestrial weathering and climate records for the early Aptian global cooling event.

Keywords Palaeoweathering, Palaeoclimate, Early Aptian global cooling, Luanping basin, Upper Xiguayuan Formation

© 2025 The Author(s). Published by Elsevier B.V. on behalf of China University of Petroleum (Beijing). This is an open access article under the CC BY license (http://creativecommons.org/licenses/by/4.0/).

Received 7 June 2024; revised 21 October 2024; accepted 22 September 2025; available online 26 September 2025

1. Introduction

The Cretaceous greenhouse represented the largest global warming event during the Phanerozoic and has been the subject of sustained attention in the geoscientific community (Haq *et al.*, 1987; Tarduno *et al.*, 1998; Cojan *et al.*, 2000; Wang *et al.*, 2014; Lv *et al.*, 2024). During the Early Cretaceous (~145.0—100.5 Ma), substantial climatic, tectonic, and eustatic changes occurred that strongly triggered perturbations in the global carbon cycle, leading to oceanic anoxic events (i.e., OAE1a, OAE1b and OAE1d; Vickers *et al.*, 2019; Jia *et al.*, 2023). The Early Cretaceous was significantly characterized by long-term greenhouse climates, with high sea levels, high atmospheric pCO_2 and a reduced equatorial to polar temperature gradient (Haq *et al.*, 1987; Huber *et al.*, 2002). However, a series of studies have revealed that the warm climate of the Early Cretaceous was punctuated by multiple global cold snaps, such as the Valanginian cold snap and the late Aptian climate cooling event (Harland *et al.*, 2007; Price and Passey, 2013; Bodin *et al.*, 2015). Both marine and terrestrial palaeoclimate records confirm that a global climate cooling event occurred in the late Aptian period (Vickers *et al.*, 2019; Jia *et al.*, 2023), and there are also marine deposits that responded to the early Aptian global cooling event (Weissert and Erba, 2004). However, the terrestrial palaeoclimate response to the early Aptian global cooling event (~120—118 Ma) has not been documented. Furthermore, the causal relationships between terrestrial palaeoclimate, continental weathering and volcanism are poorly understood. Therefore, investigating weathering and climate mechanisms during periods of climate transition is essential for addressing this gap in scientific research.

As greenhouse gas concentrations continue to increase, the current and future climates may experience recurring warming periods (Chen *et al.*, 2023). Therefore, accurate reconstruction of terrestrial weathering and the regional palaeoclimate helps trace the mechanisms of climate dynamics and provides a theoretical basis for predicting global climate change under high anthropogenic carbon conditions. However, previous studies on the palaeoclimate of sedimentary basins have been based only on qualitative analyses of arid or humid conditions through elemental geochemistry or palaeontology (Tan *et al.*, 2017; Sun *et al.*, 2022a, 2022b, 2024a; Hu *et al.*, 2023), and few reports on accurate quantitative reconstructions of regional small-scale palaeoclimates have been published (Chen *et al.*, 2021). In addition, the reconstruction of palaeoweathering and palaeoclimate via elemental geochemical methods requires systematic consideration and elimination of potential interferences on element abundances such as provenance, diagenesis (potassium metasomatism, carbonate-derived elements), sediment recycling and sedimentary sorting, which are often disregarded in previous studies. Therefore, these environmental parameters must be systematically interpreted to disentangle their respective influences and coupled interactions.

A typical case of Early Cretaceous volcanic and sedimentary strata, with a thickness of ~3200 m, is exposed in the Luanping Basin of North China. In particular, the Xiguayuan Formation of the Lower Cretaceous in the basin has continuously deposited lacustrine strata ~1700 m thick, which is an ideal interval for recording the terrestrial climate transition during the Early Cretaceous greenhouse period. During the Early Cretaceous, the Luanping Basin was subjected to frequent volcanic activity, and the continental weathering intensity and regional climate fluctuated accordingly (Pan *et al.*, 2021). However, although sporadic studies have been conducted on the palaeoclimate of the Luanping Basin (Pan *et al.*, 2021), little is known about the terrestrial palaeoweathering and palaeoclimate of the basin in the Early Cretaceous and their forcing mechanisms.

To systematically investigate terrestrial weathering and quantify the palaeoclimate during the Early

Cretaceous greenhouse period, this study provides a field section of the Yuying outcrop in the Luanping Basin. The sedimentary age of the strata in this section is early Aptian, and no detailed mineralogical or elemental geochemical studies had been conducted. We collected 16 mudstone samples and performed extensive analytical tests to characterize the chemical weathering and palaeoclimate. The scientific aims of this study are to 1) quantitatively reconstruct palaeoweathering intensity via multiple chemical weathering indices after eliminating potential interference from nonweathering factors; 2) quantitatively reconstruct palaeoclimate history, after evaluating the possible influences of carbonate-sourced elements; and 3) explore the relationship between regional palaeoclimate fluctuations and global climate changes and clarify the driving forces of regional climate fluctuations.

2. Geological setting

During the Early Cretaceous, the North China Craton (NCC) was bordered by the Central Asian Orogenic Belt (CAOB) to the north, the Qinling—Dabie—Sulu Metamorphic Belt (QDSMB) to the south, and the Pacific Convergent System (PCS) to the east (Fig. 1), with latitudes of approximately 30° N to 50° N (Menzies *et al.*, 2007; Zhang *et al.*, 2014; Qian *et al.*, 2017; Qiao *et al.*, 2022). The Early Cretaceous Luanping Basin is located on the northeastern Yanshan Belt in the NCC (Davis *et al.*, 2001; Cope and Graham, 2007; Fang *et al.*, 2022; Zhang *et al.*, 2023a) (Figs. 1 and 2A).

The Luanping Basin is a typical continental volcano-faulted lake basin that extends ~40 km in the NE—SW orientation and ~20 km in the NW—SE orientation, with a residual area of almost 800 km^2 (Pan *et al.*, 2021; Zhang *et al.*, 2023a). The basin is developed on a basement composed of Archean metamorphic and Proterozoic intrusive rocks, which are controlled mainly by the Xiaobaiqi–Fujiadian fault in the west and the Hongqi–Gangzi fault in the north, both of which are extensional normal faults (Cope *et al.*, 2010; Zhang *et al.*, 2021) (Fig. 2B). Tectonically, the Mesozoic evolution process of the Luanping Basin is divided into three stages: the first rifting stage (rift—initial), the second rifting stage (rift—climax), and the third rifting stage (rift—waning) (Wu *et al.*, 2000).

The basement of the basin is composed mainly of granite or metamorphic rocks, which are covered by nearly 5 km of Meso-Cenozoic terrestrial lacustrine clastic deposits, including Middle Jurassic, Upper Jurassic, Lower Cretaceous, and Quaternary sediments. The tectonic extension of the Early Cretaceous resulted in strong subsidence of the entire basin and widespread development of Lower Cretaceous strata (Li, 2003; Pan *et al.*, 2021), which consist of the Zhangjiagou (K_1z), Dabeigou (K_1db), Dadianzi (K_1d), and Xiguayuan (K_1x) formations, from oldest to youngest (Fig. 3A). Among them, the Zhangjiagou Formation is dominated by volcanic rocks, including tuff, trachyte and rhyolite. The Dabeigou and Dadianzi formations are composed of widely distributed fan-deltaic sandstones and lacustrine grey mudstones. The Xiguayuan Formation is dominated by conglomerates, sandstones, siltstones, mudstones and shales that are interpreted to have been deposited in alluvial fans, fan deltas, and semi-deep to deep lacustrine environments (Yan *et al.*, 2020). The total thickness of the Xiguayuan Formation, which contains a large set of thick mudstones, is ~1700 m (Pan *et al.*, 2021). This sedimentary period was characterized by strong tectonic activity, an

Fig. 1 Early Cretaceous (~120 Ma) global palaeogeographic reconstruction from Scotese (2021) showing the position of the Luanping Basin. NCC: North China Craton; CAOB: Central Asian Orogenic Belt; QDSMB: Qinling—Dabie—Sulu Metamorphic Belt; PCS: Pacific Convergent System.

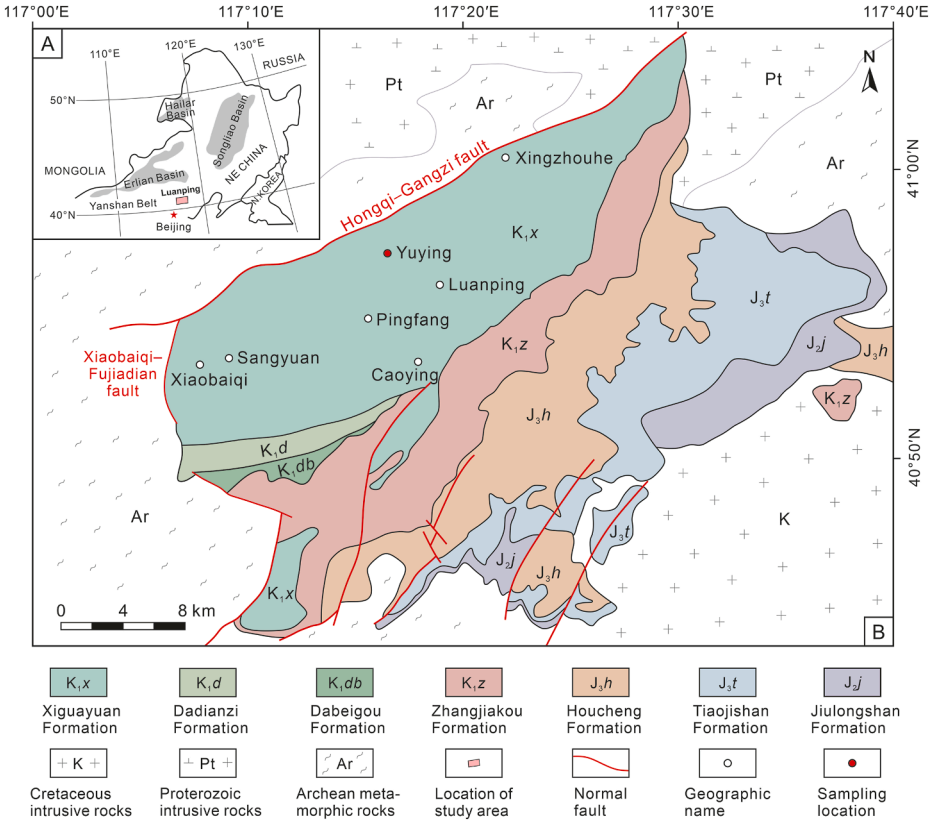

Fig. 2 Regional location (A) and simplified geological map (B) of the Luanping Basin, northeastern China (modified from Yan *et al.*, 2020; Pan *et al.*, 2021).

extensive lake basin, and abundant sources of sediment, which is ideal for exploring regional chemical weathering and climate change. The Xiguayuan Formation is further subdivided from bottom to top into lower and upper members. The lower Xiguayuan Formation has a certain hydrocarbon generation potential (Pan *et al.*, 2021), whereas the degree of organic matter enrichment in the upper Xiguayuan Formation is relatively low. The study interval in this paper is the Lower Cretaceous upper Xiguayuan Formation mudstone of the Yuying section (Fig. 3A).

The Yuying section (40°56′14.7″N, 117°16′23.6″E) is located on the northern margin of the Luanping Basin (Fig. 2B). The entire section is ~50-m thick and is mainly composed of conglomerates of varying sizes, grey sandstones and dark grey mudstones, with occasional thin layers of shales and argillaceous siltstones, which exhibit coarsening upwards (Fig. 3B). The Yuying section is composed mainly of underwater deposits at the front of the fan delta. The mudstones between the sandstones and the conglomerates are mostly dark grey and grey with a pure texture and are typical lacustrine deposits. The lower part of the Yuying section is the front fan delta with a widespread distribution of siltstones and fine sandstones, and the upper strata are alluvial fan facies with extensive development of medium—coarse conglomerates. The overall sequence is a lacustrine transgressive system domain. The dating results of existing studies on regional strata show that the alluvial fan ended at ~118.0 Ma, and the strata between its upper part and the Quaternary are missing (Wei *et al.*, 2012). The biotite $^{40}Ar/^{39}Ar$ age of the extensively developed basalts in the lower strata of the Yuying section limits the volcanic activity to ~120.0 ± 0.5 Ma (Wei *et al.*, 2012). Therefore, the age range of the Yuying section should fall between ~120.0 Ma and 118.0 Ma.

3. Sampling and methods

3.1. Sampling and experiment

The present research focused on 16 mudstone samples collected from a ~50 m thick clastic interval in the Lower Cretaceous upper Xiguayuan Formation

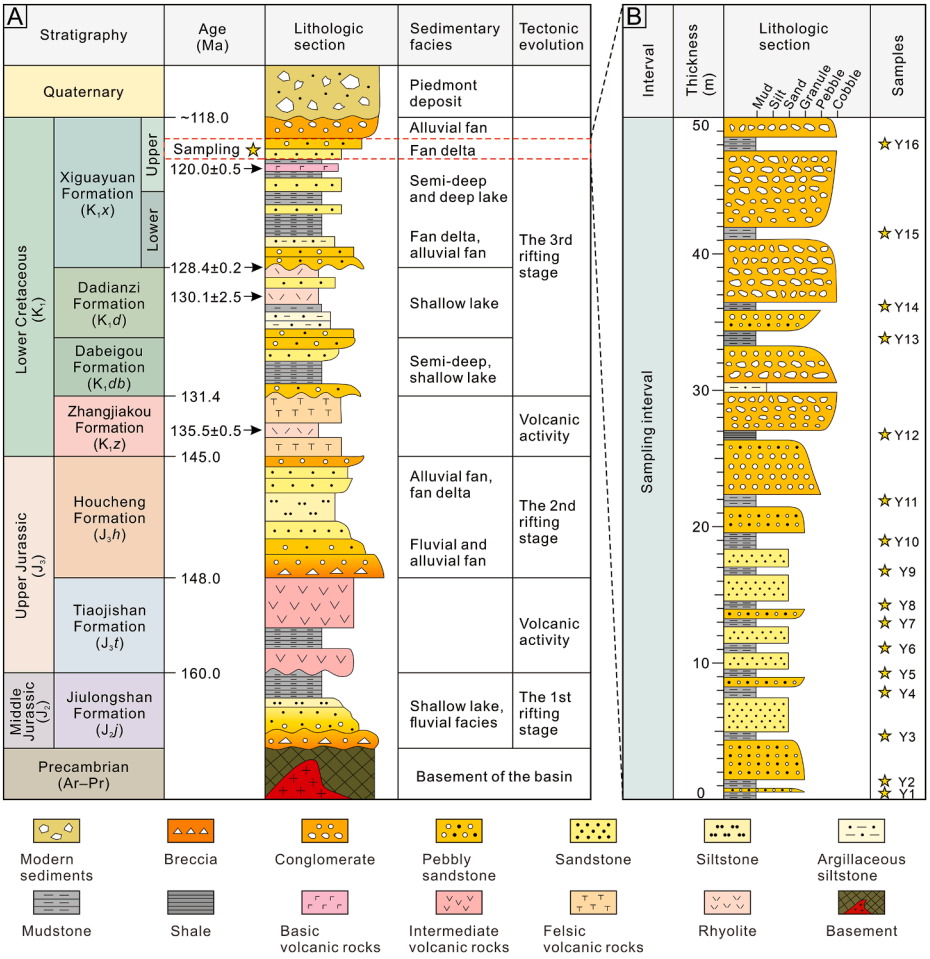

Fig. 3 **A)** Stratigraphic sequence of the Luanping Basin showing lithology, sedimentary facies and tectonic evolution (modified from Pan *et al.*, 2021); **B)** Yuying section showing lithology and sampling intervals. Ages are based on the radiometric age for the Yanshan Belt by Wei *et al.* (2012).

of the Yuying section (Fig. 2B and 3B). The samples were collected from the grey mudstone interlayers between the sandstones and the conglomerates at approximately equal intervals, which can accurately reflect the subtle changes in palaeoenvironmental sensitivity. From the bottom to the top, we numbered the samples from Y1 to Y16 (Fig. 3B). All samples were obtained from fresh mudstone sections after the weathering surface was broken. The lithology of the samples is fine-grained pure lacustrine mudstone. For these samples, we performed a total of 16 X-ray diffraction (XRD) analyses of mineral contents, 16 X-ray fluorescence (XRF) analyses of major element concentrations and 16 inductively coupled plasma–mass spectrometry (ICP–MS) analyses of trace and rare earth element concentrations. All the samples used for these experimental analyses were cut from fresh segments and swilled with clean water to remove mud-stained surfaces before these tests.

The mineral compositions were quantitatively determined via a Rigaku Ultima IV X-ray diffractometer. All mudstone samples were ground into powder and sieved to a size of 200 mesh (<75 μm). Each sample was evenly divided into two parts, one of which was directly used to determine the composition of the whole-rock minerals, including the total amounts of clay minerals and the contents of nonclay minerals such as quartz, feldspar, and mica. For the other half, particles with a size of <2 μm were collected through gravitational sedimentation following Stokes' Law to determine the relative content of each type of clay mineral (Ye *et al.*, 2016). All the powdered samples were dried at 50 °C for 48 h and cooled to room temperature. Subsequently, approximately 40 mg of the sample was placed in a beaker and stirred with 0.7 ml of 25% H_2O_2. The dispersed suspension was subsequently poured onto a glass slide and was air-dried to obtain air-dried (AD) samples. Diffractograms of the

AD samples were measured on an X-ray diffractometer (Cu—Kα, 40 kV, 40 mA, 2°—60°, step 0.02°, and 2°/min). Next, the AD samples were treated with ethylene glycol vapour at 50 °C for 8 h and placed on a diffractometer with the same parameters to obtain the diffractograms of the ethylene glycol-saturated (EG) samples. The EG samples were heated at a high temperature of 500 °C for 2 h to obtain the heated (T) diffractograms. For each sample, the XRD pattern includes the air-dried (AD), glycol-saturated (EG), and heated (T) diffractograms (Fig. 4). The quantitative analysis of relative mineral contents was performed via *JADE* 6.5 software, which calculates these contents on the basis of the peak heights and areas of basal reflections for minerals observed in the diffractograms.

An Axios mAX XRF spectrometer was used to determine the concentrations of major elements via the glass melting method. Prior to XRF analysis, the mudstone samples were ground into powder via an agate mortar and sieved through a 200-mesh (75 μm) sieve. Subsequently, 0.5 g of dried sample material was weighed into a porcelain crucible and then treated with 4 g of $Li_2B_4O_7$ and a drop of cosolvent (2% LiBr—1%NH_4I). Next, the treated samples were placed on an electric heating plate for thorough drying and then melted in propane-rich carrier gas at a high temperature of approximately 1200 °C for 15 min via an automatic flame melting machine. Ultimately, the concentrations of major elements in the molten samples were determined via an XRF spectrometer. The relative standard deviations (RSDs) in replicate measurements for the XRF analyses were usually less than 5%.

Trace elements were analysed via a NexION 300D ICP–MS spectrometer. Similarly, the sample was thoroughly crushed and sieved to 200 mesh (<75 μm), and then dried at 700 °C for 3 h to completely remove organic matter. After it was cooled to room temperature, 50 mg of dried powdered sample was placed in a Teflon container and digested with a mixture of 2 ml 65%HNO_3 and 5 ml 40%HF. The accuracy of the measurements was verified with standard materials and duplicate samples.

3.2. Analytical procedures

3.2.1. Chemical weathering indices

In this study, various chemical weathering indices, such as the chemical index of alteration (CIA;

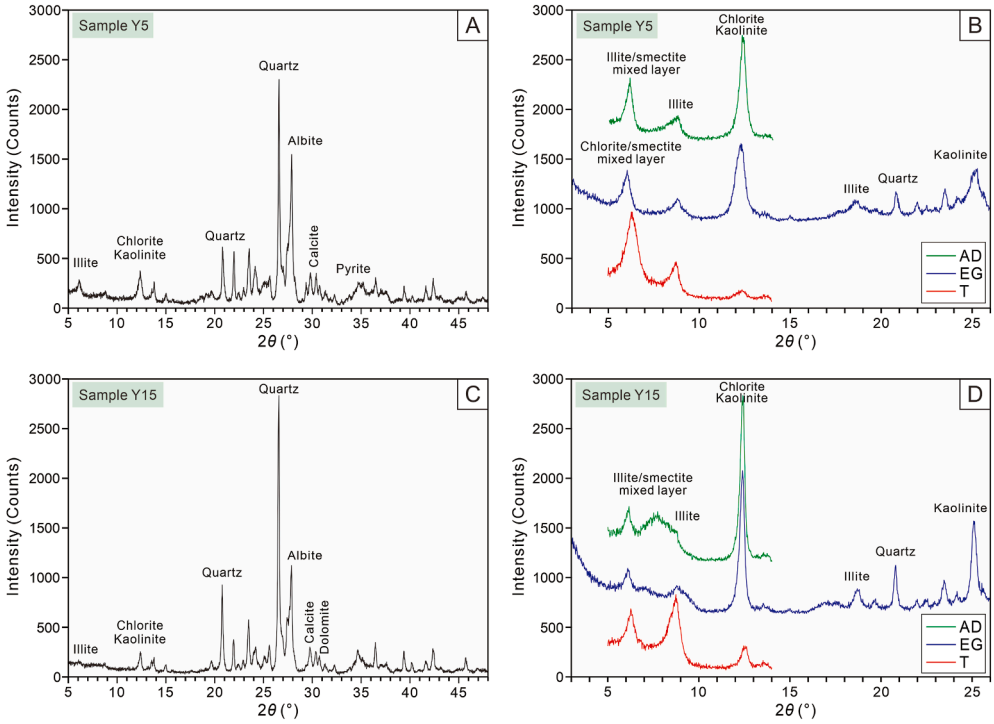

Fig. 4 XRD patterns of two representative samples in the study interval. **A)** Whole-rock mineral composition of bulk sample Y5 with quartz, albite, clay, calcite and pyrite; **B)** Clay mineral composition of clay-sized sample Y5 with chlorite/smectite mixed layer, illite/smectite mixed layer, illite, chlorite and kaolinite; **C)** Whole-rock mineral composition of bulk sample Y15 with quartz, albite, clay, calcite and dolomite; **D)** Clay mineral composition of clay-sized sample Y15 with illite/smectite mixed layer, illite, chlorite and kaolinite. AD: air-dried sample; EG: glycol-saturated sample; T: heated sample.

Nesbitt and Young, 1982), chemical index of weathering (CIW; Harnois, 1988), chemical index of alteration that does not consider CaO (CIX; Dinis *et al.*, 2017), plagioclase index of alteration (PIA; Fedo *et al.*, 1995), weathering index of Parker (WIP; Parker, 1970), and sodium depletion index (τ_{Na}; Anderson *et al.*, 2002), were used to track the intensity of chemical weathering.

The CIA is expressed as the molar percentage of $Al_2O_3/(Al_2O_3 + CaO^* + Na_2O + K_2O) \times 100$ (Nesbitt and Young, 1982). CaO* is the molar percentage of CaO derived solely from silicate minerals on the basis of the correction method proposed by McLennan (1993). Previous studies have indicated that CIA values > 80, 60—80 and 40—60 represent strong, moderate and weak weathering, respectively (Bomou *et al.*, 2013). The CIW, calculated as the molar percentage of $Al_2O_3/(Al_2O_3 + CaO^* + Na_2O) \times 100$ (Harnois, 1988), was proposed to eliminate the interference of K increased by K-metasomatism. The CIX was selected to avoid anomalies caused by the presence of carbonate minerals, expressed as the molar ratio of $Al_2O_3/(Al_2O_3 + Na_2O + K_2O) \times 100$ (Garzanti *et al.*, 2014; Dinis *et al.*, 2017). The PIA was proposed to determine the weathering intensity of plagioclase, expressed as the molar percentage of $(Al_2O_3 - K_2O)/(Al_2O_3 + CaO^* + Na_2O - K_2O) \times 100$ (Fedo *et al.*, 1995). In addition to the molar ratio of major elements, the bond strengths between elements and oxygen were employed as weighting factors in the weathering index. The WIP was formulated as $(CaO^*/0.7 + 2Na_2O/0.35 + 2K_2O/0.25 + MgO/0.9) \times 100$ (Parker, 1970). This formula measures the intensity of weathering a rock has undergone compared with that of the parent rock and its susceptibility to further weathering. A low WIP indicates a lower alkali metal content, which in turn indicates a strong weathering process. Furthermore, τ_{Na} has also been used to indicate the intensity of chemical weathering in source areas, which reflects the loss and gain of Na and is expressed as $(Na_{mud}/Zr_{mud})/(Na_{source}/Zr_{source}) - 1$ (Anderson *et al.*, 2002; Rasmussen *et al.*, 2011). Here, Na_{mud}, Zr_{mud}, Na_{source}, and Zr_{source} refer to the Na content in mudstone samples, the Zr content in mudstone samples, the Na content in the NCC, and the Zr content in the NCC, respectively.

3.2.2. Palaeoclimate reconstruction methods

The Sr/Cu ratio is a commonly used a proxy for reconstructing palaeoclimates, with a threshold of 10, to distinguish between humid climates and arid climates (Liu and Zhou, 2007). The Rb/Sr ratio is also susceptible to climate change because of the high stability of Rb and the low stability of Sr during weathering (Chen *et al.*, 2000). Therefore, a high Rb/Sr ratio corresponds to a humid climate with strong weathering, whereas a low value reflects drought. In addition, the C value is also a reliable proxy for restoring palaeoclimates; and it is expressed as $\Sigma(Fe + Mn + Cr + Ni + V + Co)/\Sigma(K + Na + Ca + Mg + Sr + Ba)$ (Zhao *et al.*, 2007). All the elements are expressed in parts per million. Typically, C values less than 0.6 correspond to arid and semiarid climates, whereas C values greater than 0.6 indicate humid climates (Ma *et al.*, 2023).

The CIA values of modern large river mouth suspended sediments are particularly sensitive to land surface temperature (LST) and latitude (Li and Yang, 2010). Yang *et al.* (2014) proposed an empirical relationship between the CIA and LST as a thermometer, expressed as $LST = 0.56 \times CIA - 25.7$ ($R^2 = 0.5$). This formula is applicable to the temperature range of 3 °C—25 °C, with an error of approximately ±5 °C, corresponding to a CIA value range of ~50—90 (Sun *et al.*, 2022c). Like the CIA value for the LST, the τ_{Na} index of the surface soil chemical weathering intensity is also highly sensitive to the mean annual temperature (MAT). The transfer function between τ_{Na} and MAT as a palaeothermometer was quantified as $MAT = -24.2 \times \tau_{Na} - 0.9$ (Yang *et al.*, 2016a).

4. Results

4.1. Mineralogy and lithology

The XRD results are shown in Supplementary Tables S1 and S2. The relative contents of plagioclase and quartz have large distributions of 25.4%—49.6% and 27.0%—46.6%, with average values of 36.0% and 33.5%, respectively. The relative contents of clay minerals and K-feldspar are similar, varying from 7.6% to 25.4%, with a mean value of 14.8%, and from 4.2% to 15.3%, with an average value of 9.4%, respectively. The relative contents of calcite, dolomite and pyrite are relatively low (mean contents less than 5%) (Supplementary Table S1). Among the clay minerals, the relative content of mixed-layer chlorite/smectite (C/S) is the highest, varying from 0 to 81.4%, with an average value of 32.6%; the relative content of chlorite (C) is the second highest, varying from 1.2% to 50.0%, with a mean value of 26.6%. The contents of illite (I), mixed-layer illite/smectite (I/S), and kaolinite (K) are relatively low, ranging from 6.3% to 26.4%, 1.2%—51.5% and 0.8%—30.9%, with average values of 15.1%, 12.5% and 13.2%, respectively (Supplementary Table S2).

The position of the mudstone samples in the ternary diagram (Fig. 5) shows that most of them are clay-rich siliceous mudstones with a silica-dominated lithotype, with only one sample located in the area where mixed siliceous mudstones are present. The variation amplitudes of the total clay minerals in the mudstone samples are slightly greater than those of the total carbonate minerals (calcite and dolomite). Overall, the mineral compositions of the samples exhibit slight variability and are dominated by fine-grained siliceous lithotypes (Fig. 5; Supplementary Table S1).

4.2. Palaeoweathering intensity

In this study, we combine CIA, CIW, CIX, PIA, WIP, and τ_{Na} to quantify the chemical weathering intensity experienced by the sources to the mudstones in the study interval. Notably, although minerals such as quartz and calcite have a significant effect on the contents of Ca, Na, Al, K and other elements related to the weathering index, all samples are fine-grained siliceous mudstones with weak differences, so the influence of mineral composition can be disregarded. On the basis of the percentage contents of major elements (Supplementary Table S3) and the calculation formula provided above, the geochemical weathering index values of the upper Xiguayuan Formation mudstone samples in the Luanping Basin are shown in Fig. 6.

The CIA values range from 55.8 to 68.4, with an average value of 62.0, indicating a weak to moderate weathering intensity (Fig. 6A). The CIW values range from 65.0 to 83.6, with an average value of 74.2 (Fig. 6B). The CIX values vary from 62.6 to 69.4, with a mean value of 66.2, and most CIX values are concentrated at approximately 65 (Fig. 6C). The highest, lowest, and average values of the PIA in the study interval were 79.0, 58.0, and 68.1, respectively (Fig. 6D). The CIA, CIW, CIX and PIA values are similar, which implies that the source area has experienced weak to moderate weathering intensity. The WIP values of all the mudstone samples in the study interval range from 47.8 to 56.3, with a mean of 52.6, which is the opposite of the trend for the four weathering indices mentioned above, but all the samples have weak to moderate weathering degrees (Fig. 6E). Moreover, the range of τ_{Na} in the study interval is −0.39 to 0.11, with an average of −0.16. Only 4 samples have τ_{Na} values higher than 0, whereas all other samples exhibit Na loss (Fig. 6F). With the exception of slightly abnormal samples such as Y8 and Y9, the variation in τ_{Na} shows an opposite trend to that of CIA, CIW, CIX, and PIA but is similar to the variation trend of WIP.

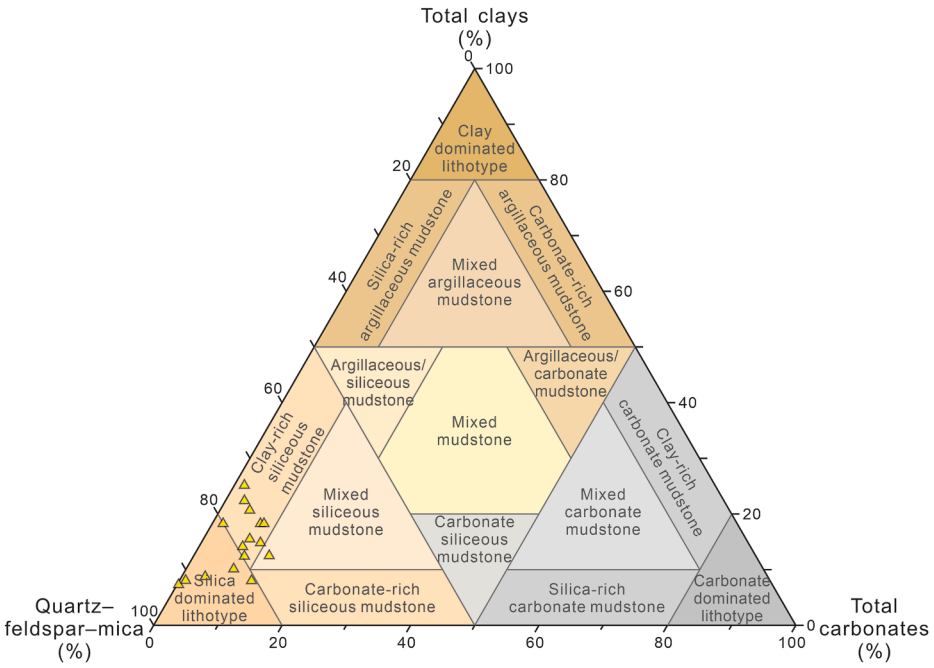

Fig. 5 Ternary diagrams showing the mineral composition distribution of the mudstone samples (yellow triangles) from the upper Xiguayuan Formation, Yuying section, Luanping Basin (modified after Liu *et al.*, 2020; Cai *et al.*, 2023; Ma *et al.*, 2023. See Supplementary Table S1 for the compositional values).

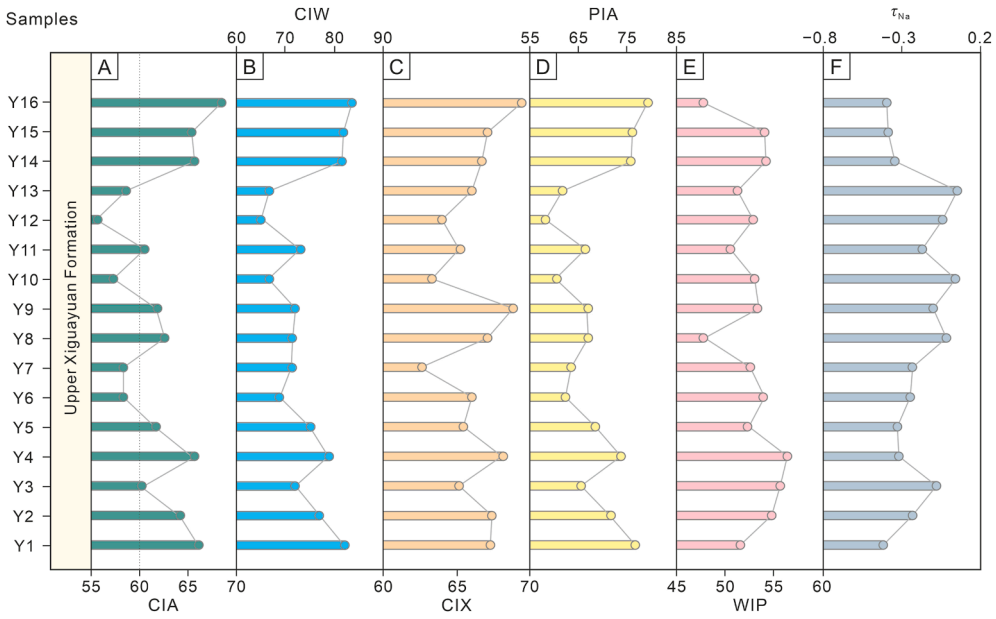

Fig. 6 Vertical variations in weathering index values for the mudstone samples of the upper Xiguayuan Formation, Yuying section, Luanping Basin. CIA = chemical index of alteration (Nesbitt and Young, 1982); CIW = chemical index of weathering (Harnois, 1988); CIX = chemical index of alteration that does not consider CaO (Garzanti *et al.*, 2014); PIA = plagioclase index of alteration (Fedo *et al.*, 1995); WIP = weathering index of Parker (Parker, 1970); τ_{Na} = sodium depletion index (Anderson *et al.*, 2002). See Supplementary Table S3 for the source data.

4.3. Palaeoclimate characteristics

4.3.1. Arid or humid conditions

We systematically determined the trace element contents of 16 mudstone samples from the upper Xiguayuan Formation in the Luanping Basin (Supplementary Table S4) and established a Sr—Cu cross-plot based on these data (Fig. 7A). In the study interval, the Sr mass fraction ranged from 178.0 ppm to 759.0 ppm, with an average value of 406.1 ppm; and the Cu content ranged from 8.4 ppm to 24.8 ppm, with an average of 14.9 ppm. The Sr/Cu ratios range between 10.4 and 69.0, with an average value of 30.3, suggesting arid climatic conditions (Fig. 7A). The Rb mass fraction ranges from 97.4 ppm to 158.0 ppm, with a mean of 127.6 ppm. The Rb/Sr ratios range 0.16—0.89, with an average ratio of 0.40, plotting the majority samples in the arid zone and only a few in the humid zone (Fig. 7B). The Rb/Sr ratios exhibit a similar systematic trend to that of the Sr/Cu ratios.

In addition, we also calculated the C-value used to distinguish climate conditions. The C-value of the study interval ranges from 0.33 to 0.51, with an average value of 0.42, indicating that the climate conditions range from semiarid to arid (Fig. 7C). Moreover, the intersection plots of Rb/Sr versus Sr/Cu indicate a good correlation, with a correlation coefficient of 0.89 (Fig. 7D). The correlation between the C-value and the Sr/Cu ratio is weak, with a correlation coefficient of 0.39, reflecting a consistent trend of climate aridification (Fig. 7E). Unlike the above relationship, there is almost no correlation between the C-value and the Rb/Sr ratio, with a correlation coefficient of only 0.11 (Fig. 7F). Nevertheless, all three climate proxies indicate an arid environment.

4.3.2. Palaeotemperature

In this study, the land surface temperature (LST) and mean annual temperature (MAT) of the upper Xiguayuan Formation were estimated. The LSTs, calculated from CIA values, range from 5.5 °C to 12.6 °C, with a mean of 9.0 °C, while the MATs are from −3.7 °C to 8.6 °C, with a mean of 2.9 °C, converted from τ_{Na} values (Fig. 8; Supplementary Table S3).

5. Discussion

5.1. Interferences of nonweathering factors on weathering indices

The various chemical weathering indices applied in this paper have their respective applicability and inferiority. CIW only makes a simple deduction for K_2O and disregards the Al in K-feldspar, whereas CIX

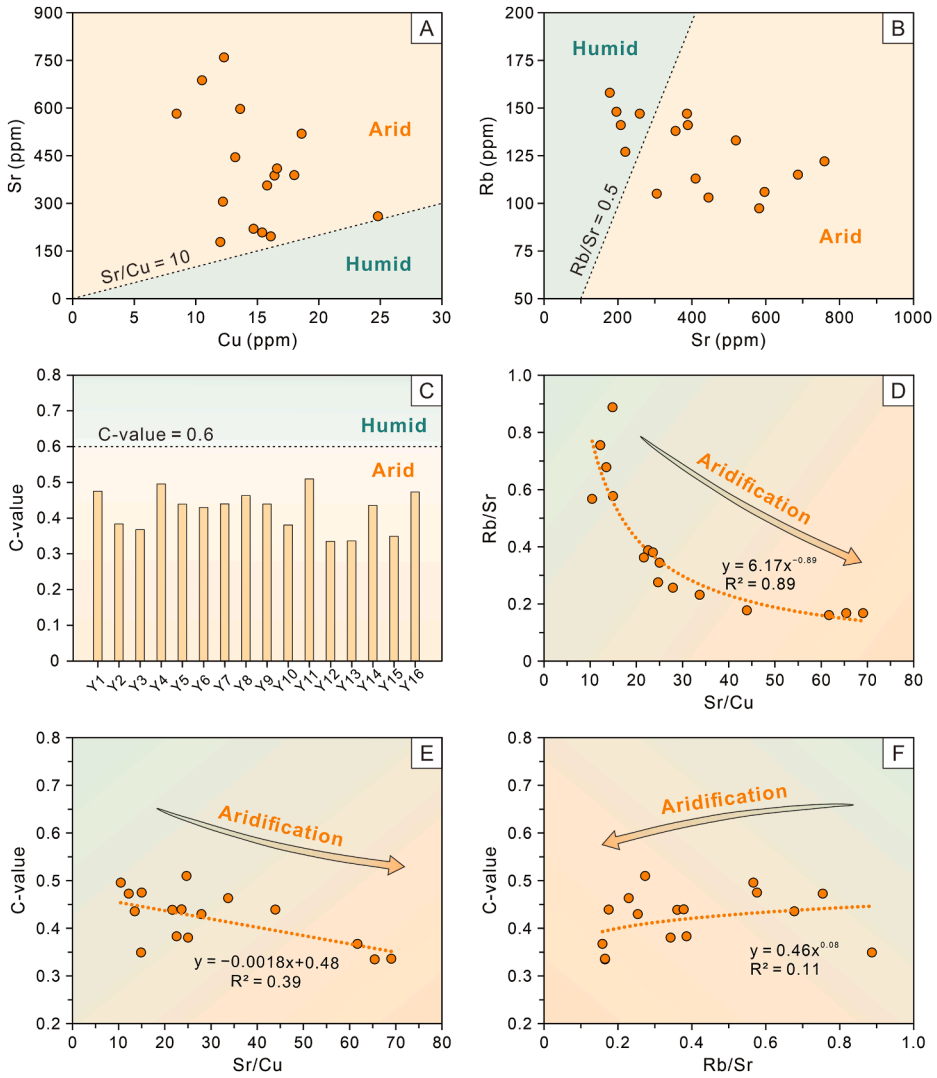

Fig. 7 Cross-plots of **A)** Sr versus Cu, **B)** Rb versus Sr, **C)** C-value versus sample ID, **D)** Rb/Sr versus Sr/Cu, **E)** C-value versus Sr/Cu, and **F)** C-value versus Rb/Sr for identifying climate conditions in the study interval. See Supplementary Table S4 for the source data.

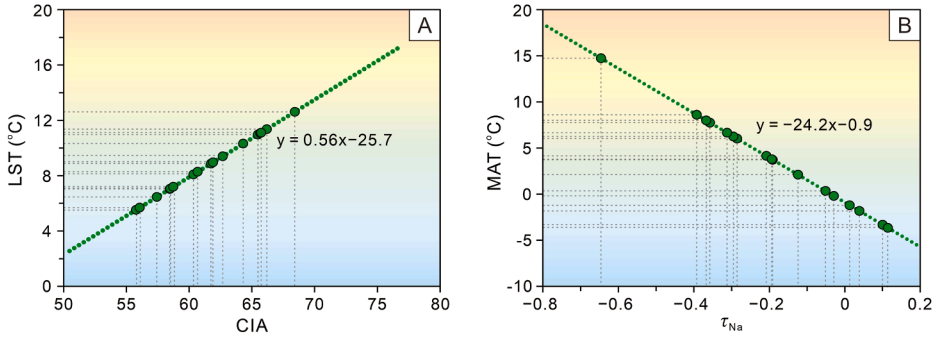

Fig. 8 Cross-plots of **A)** LST versus CIA, and **B)** MAT versus τ_{Na} for calculating palaeotemperature in the upper Xiguayuan Formation, Yuying section, Luanping Basin. See Supplementary Table S3 for the source data.

deducts CaO to exclude the heterogeneity of Ca, disregarding Ca weathering. The PIA removes K_2O and Al_2O_3 from K-feldspar and is only applicable for determining the degree of weathering in source areas where the parent rock contains only plagioclase and not potassium feldspar. Similarly, τ_{Na} considers only the loss and gain of Na while disregarding other alkali metal elements. Previous studies have shown that after nonweathering factors are eliminated, the CIA and WIP are the most reliable weathering indicators (Yang and Du, 2017; Lv *et al.*, 2022). The chemical weathering of terrestrial environments is predominantly controlled by temperature and moisture conditions (Sheldon and Tabor, 2009). Clay minerals cause changes in the chemical composition of fine-grained sediments during diagenetic evolution, such as K-metasomatism in kaolinite (Fedo *et al.*, 1995; Rieu *et al.*, 2007). Among all nonweathering interference factors, the CIA is sensitive to K-metasomatism during diagenesis, whereas the WIP is influenced mainly by sediment source composition (Yang *et al.*, 2020; Lv *et al.*, 2022).

5.1.1. Diagenesis

Burial diagenesis has an impact on the element content of clay by altering the relative proportion of clay minerals (Ye *et al.*, 2016). The conversion of smectite to illite or chlorite with increasing burial depth is prevalent diagenetic change (Chamley, 1994; Ye *et al.*, 2016). The relatively low proportion of smectite in the chlorite—smectite mixed layer of the study interval may indicate strong burial diagenesis. However, the high proportion of smectite (Y1 and Y14) in the chlorite—smectite mixed layer exhibits extremely similar element content characteristics to the relatively low proportion of smectite (Supplementary Tables S3—S5), indicating that burial diagenesis has a weak impact on element content.

In this study, the weathering trend of the samples in the Al_2O_3—(CaO^*+Na_2O)—K_2O (A—CN—K) ternary diagram is parallel to that of the NCC and tends towards the K_2O apex (Fig. 9A), indicating the rationality of the upper Xiguayuan Formation source and the presence of K-metasomatism. Previous studies have shown that K enrichment caused by the conversion of kaolinite to illite can force samples to plot towards the K_2O apex of the A—CN—K triangle, accompanied by lower CIA values and higher WIP values (Fedo *et al.*, 1995; Lv *et al.*, 2022). Therefore, the elimination of K-metasomatism is used to restore the original weathering trend of each mudstone sample, thereby obtaining corresponding CIA and WIP values.

In accordance with the methods of Panahi *et al.* (2000), the CIA values were corrected to the CIA* values through K-metasomatism on the A—CN—K ternary diagram. The range of CIA* values is 56.5—72.8, with an average of 64.4 (Fig. 9B). On the basis of the corrected A—CN—K ternary diagram, the corrected K_2O contents were used to calculate the corrected WIP (WIP*) values, which range from 37.6 to 53.3, with an average value of 45.8. The CIA* and WIP* values, which eliminate the interference of K-metasomatism during diagenesis, are used to accurately quantify palaeoweathering and palaeotemperature.

5.1.2. Provenance

Element enrichment in sediments varies with changes in provenance, but most immobile elements undergo minor losses during chemical weathering

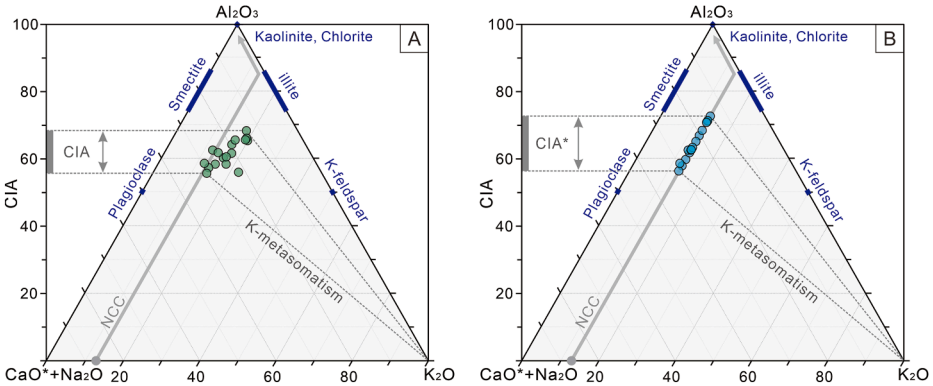

Fig. 9 Geochemical weathering trends of the upper Xiguayuan Formation mudstones, Yuying section, Luanping Basin. **A)** Ternary diagram of Al_2O_3—(CaO^*+Na_2O)—K_2O (A—CN—K), based on the method proposed by Nesbitt and Young (1989); **B)** Corrected ternary diagrams of A–CN–K, based on the method proposed by Fedo *et al.* (1995) and Panahi *et al.* (2000). CIA* = corrected chemical index of alteration; NCC = North China Craton. See Supplementary Table S3 for the source data.

(Yang *et al.*, 2016a; Lv *et al.*, 2022). Our geochemical data indicate the similarity in element abundance between the upper Xiguayuan Formation mudstones and the average concentration of the NCC proposed by Gao *et al.* (1998), which represents the consistency and stability of the source composition (Supplementary Tables S3—S5). The contents and associated geochemical parameters of rare earth elements (REEs) in the samples, Upper Continental Crust (UCC), NCC, and chondrite are listed in Supplementary Table S5. The results indicate that the REEs contents of all the samples are slightly greater than those in the UCC and NCC. The total REE (ΣREE) contents vary from 176.71 ppm to 263.43 ppm, with a mean value of 215.62 ppm. Light rare earth elements (LREEs) refer to La, Ce, Pr, Nd, Sm, and Eu, whereas heavy rare earth elements (HREEs) are the rest rare earth elements. The LREEs/HREEs ratios range between 10.11 and 12.64, with a mean value of 10.99, which is higher than the UCC value of 9.33. The chondrite-normalized REE pattern is characterized by sloping LREEs and flat HREE trends, accompanied by weak Eu anomalies (Fig. 10). The calculated data in Supplementary Table S5 are highly consistent with the chondrite-normalized REE pattern, indicating the typical characteristics of high LREE enrichment and slight HREE enrichment. This result is similar to the result obtained by Pan *et al.* (2021) from hydrocarbon source rocks in the upper Xiguayuan Formation of the Luanping Basin.

Although such subtle changes in provenance hardly interfere with chemical weathering, the degree of interference still needs to be accurately evaluated (Lv *et al.*, 2022). The Al_2O_3/TiO_2 ratio is a sensitive geochemical proxy that is extensively utilized to identify source rock composition (Yang *et al.*, 2018; Qadrouh *et al.*, 2021). The chemical principle of using this ratio for source composition discrimination is that Al_2O_3 is enriched in felsic minerals, whereas TiO_2 accumulates in mafic minerals. During the transport of Al- and Ti-rich terrestrial minerals, Al and Ti remain almost unchanged, and the fractionation of the Al_2O_3/TiO_2 ratio can be disregarded (Yamamoto *et al.*, 1986; Moosavirad *et al.*, 2011). There is no explicit correlation between CIA* values and Al_2O_3/TiO_2 ratios (R^2 = 0.001), indicating that the variations in CIA* values were not affected by sedimentary provenance (Fig. 11A). In addition, the correlation between WIP* and Al_2O_3/TiO_2 is also weak, with a correlation coefficient R2 of only 0.07, indicating that the interference of provenance with chemical weathering can be completely disregarded (Fig. 11B).

The Zr/Ti ratio, similar to the Al_2O_3/TiO_2 ratio, is also commonly employed as an important proxy for inferring the composition of source rocks, as Zr and Al_2O_3 are similar and are enriched mainly in felsic minerals (Tao *et al.*, 2017; Qi *et al.*, 2020). The Zr/Ti ratio is not significantly different between the UCC and the NCC and tends to be flat with small

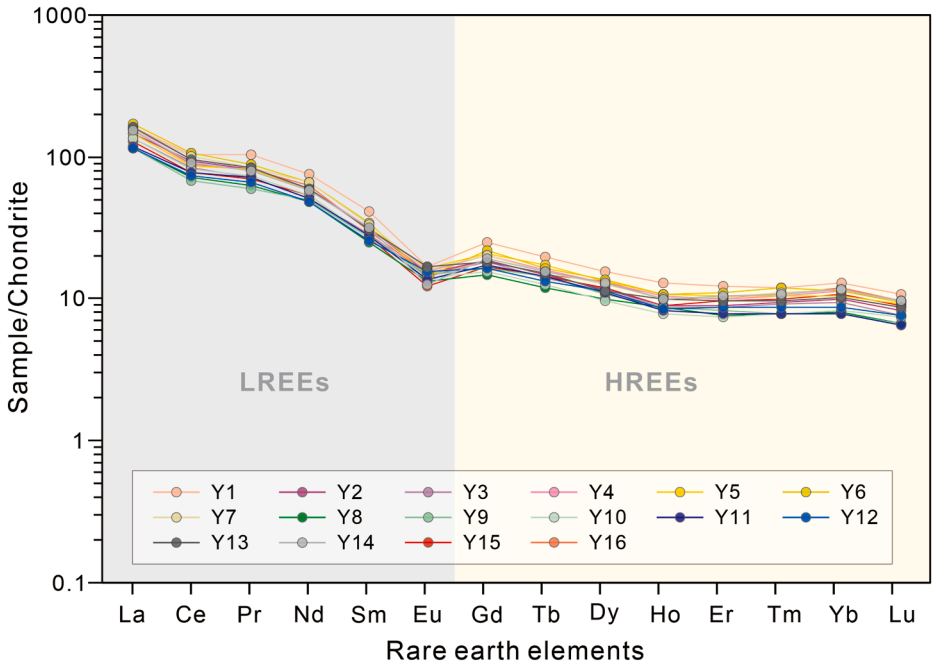

Fig. 10 Chondrite-normalized REE patterns of the mudstone samples from the upper Xiguayuan Formation, Yuying section, Luanping Basin, showing sloping LREEs and flat HREE trends, with weak Eu anomalies. The chondrite normalization values are derived from Taylor and McLennan (1985). Source data are provided in the Supplementary Table S5.

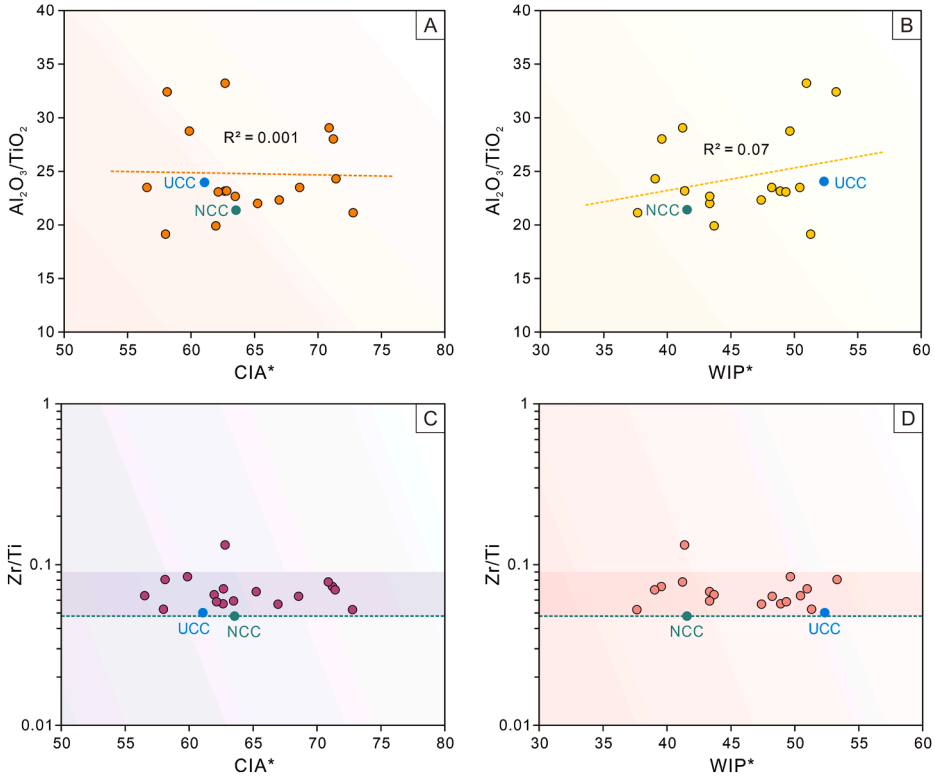

Fig. 11 Cross-plots of **A)** Al_2O_3/TiO_2 versus CIA*, **B)** Al_2O_3/TiO_2 versus WIP*, **C)** Zr/Ti versus CIA*, and **D)** Zr/Ti versus WIP* for identifying the interference of provenance in the upper Xiguayuan Formation, Yuying section, Luanping Basin. WIP* = corrected weathering index of Parker, CIA* = corrected chemical index of alteration. See Supplementary Table S3 for the source data.

fluctuations. Notably, the CIA* and WIP* values have no significant correlations with the Zr/Ti ratios (Fig. 11C and D), which contradicts the speculation that chemical weathering indices are affected by provenance.

5.1.3. Sediment recycling

Previous studies have shown that zircon accumulates during sediment recycling, thereby diluting other mineral components and corresponding chemical components (Cox *et al.*, 1995; Armstrong-Altrin *et al.*, 2004). Therefore, sediment recycling significantly affects the chemical composition of detrital rocks (Lv *et al.*, 2022). As sediment recycling progresses, the WIP decreases linearly because of the removal of CaO, Na_2O, K_2O, and MgO, whereas the CIA is not affected by this process because it is calculated using molar ratios that contain the stable Al_2O_3 (Parker, 1970; Garzanti *et al.*, 2014; Lv *et al.*, 2022). The intersection plot of the WIP* and CIA* values of the samples indicates a correlation (R^2 = 0.63) between the two weathering indices, which is highly consistent with the predicted NCC weathering trend (Fig. 12A). A significant difference exists between the distribution of samples with trends parallel or close to the NCC weathering trend and the longitudinal distribution of sediment recycling. This difference eliminates the potential interference of sediment recycling on the weathering signals.

A bivariate plot of Th/Sc versus Zr/Sc is also widely utilized to evaluate possible sediment recycling because the Zr/Sc ratios increase with increasing zircon addition during recycling, whereas the Th/Sc ratios remain relatively constant (Roddaz *et al.*, 2005). The samples exhibit a trend similar to that of the normal composition variations, with almost no right-leaning sediment recycling (Fig. 12B). Thus, these mudstones have not undergone weathering, erosion, transport, or redeposition after sedimentation or diagenesis.

5.1.4. Sedimentary sorting

Numerous studies have shown that stable minerals such as quartz and zircon are enriched in coarse-grained sediments during the sedimentary sorting process, whereas clay minerals are enriched in residual fine-grained sediments (Roddaz *et al.*, 2006;

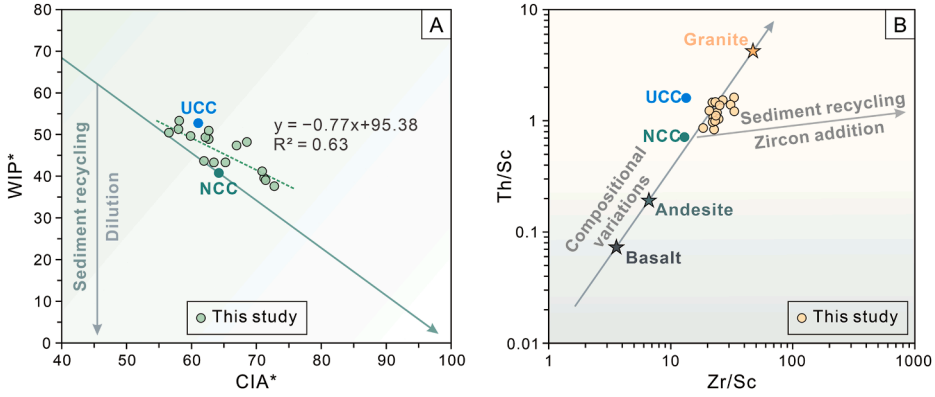

Fig. 12 Cross-plots of **A)** WIP* versus CIA* (modified after Lv *et al.*, 2022), and **B)** Th/Sc versus Zr/Sc ratios (modified after McLennan, 1993) for identifying the interference of sediment recycling in the samples of the upper Xiguayuan Formation, Yuying section, Luanping Basins. CIA* = corrected chemical index of alteration; WIP* = corrected weathering index of Parker. See Supplementary Tables S3 and S4 for the source data.

Lv *et al.*, 2022). The changes in mineral proportions caused by sorting lead to corresponding variations in chemical composition, which affect the accuracy of weathering indices. Previous studies on sedimentary facies in the study area have shown that the upper Xiguayuan Formation sandstones are typical fan deltas dominated by gravity flows (Yan *et al.*, 2020; Zhang *et al.*, 2023a). The small scale of the lake basin implies that the mudstone also had a palaeogeographic background of rapid sedimentation near the provenance, with weak sedimentary sorting. The Al_2O_3/SiO_2 ratio is widely employed to quantify the potential impact of sorting on weathering indices (Yang *et al.*, 2016a; Lv *et al.*, 2022). The intersection diagrams of the Al_2O_3/SiO_2 ratio versus the CIA* and the WIP* values reveal that the sedimentary sorting process itself is weak and poorly correlated with weathering indices (Fig. 13). Therefore, the interference of weathering from sedimentary sorting can be disregarded.

5.2. *Influences of carbonate-sourced elements on palaeoclimate proxies*

5.2.1. *Influence of carbonate Sr on bimetallic proxies*

A crucial issue in using sediment Sr/Cu and Rb/Sr ratios as palaeoclimate proxies is the potential alteration of clay component signals by carbonate-sourced Sr, as residual Sr in carbonate rocks interferes with adsorbed Sr in experimental results (Wei and Algeo, 2020; Sun *et al.*, 2024b). The high Sr content of carbonate sources can easily be mistaken for Sr adsorbed by clay minerals and can be used to calculate Sr/Cu and Rb/Sr ratios, ultimately increasing the Sr/Cu ratio and decreasing the Rb/Sr ratio in sediments (Sun *et al.*, 2024a). Therefore, evaluating samples affected by carbonate-sourced Sr is essential. In this study, we used CaO as a proxy for carbonate content.

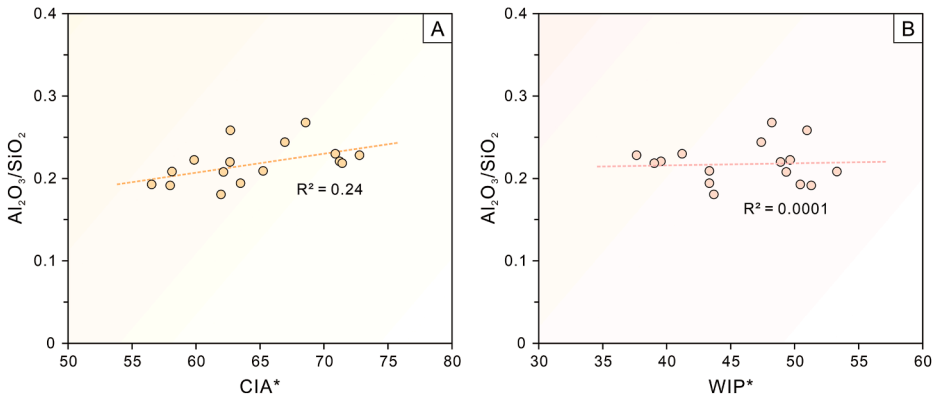

Fig. 13 Cross-plots of **A)** Al_2O_3/SiO_2 versus CIA* and **B)** Al_2O_3/SiO_2 versus WIP* for identifying the interference of sorting in the mudstone samples of the upper Xiguayuan Formation, Yuying section, Luanping Basins. CIA* = corrected chemical index of alteration; WIP* = corrected weathering index of Parker. See Supplementary Table S3 for the source data.

According to the test results, there is a positive correlation between Sr and CaO (R^2 = 0.66) (Fig. 14A), which may indicate that the Sr in the study interval was strongly affected by the interference of carbonate sources. However, it is difficult to determine an appropriate CaO threshold to eliminate samples affected by carbonate-sourced Sr.

Previous studies have evaluated bulk Sr, residual Sr, and acidic Sr in detail through leaching experiments for fine-grained lacustrine sediments and case studies, indicating that carbonate-derived Sr can also serve as a suitable proxy for weathering and climate (Yang *et al.*, 2016b, 2016c). The Sr in this study refers to bulk Sr. The high correlation between Sr and CaO indicates a considerable proportion of carbonate sources. Therefore, this study disregards the difference between clay-adsorbed Sr and carbonate-derived Sr, but the accuracy of the proxy based on bulk Sr should be confirmed. In addition, since the provenance, sorting and sediment recycling of the samples themselves are relatively weak, the impacts on palaeoclimate proxies have not been considered.

5.2.2. *Influence of carbonate Ca on C-values*

Previous studies have confirmed that calcium from carbonate sources can interfere with weathering assessment; therefore, CaO* was used to represent Ca only from silicate rocks (McLennan, 1993). However, the carbonate-sourced Ca in the C-value calculation formula has not been eliminated in all previous studies. Similarly, the potential impact of K-metasomatism was not considered in the calculation of the C-value. On the basis of the C-values, we developed a corrected C-value (C-value*) to accurately represent the palaeoclimate, which requires the use of the previously mentioned error elimination method to eliminate the interference of carbonate-source Ca and K-metasomatism. The C-values and C-values* indicate climate conditions ranging from semiarid to arid (Fig. 14B). Moreover, the intersection plots of C-value* versus Sr/Cu and C-value* versus Rb/Sr indicate good correlations among the three palaeoclimate proxies, with correlation coefficients of 0.63 and 0.43, respectively (Fig. 14C and D). Compared with the C-value, the C-value* clearly increases its correlation with bimetallic proxies (Fig. 7E and F), providing reliable evidence for several palaeoclimate proxies.

5.3. *Implications for an early Aptian global cooling*

Chemical weathering indices can not only reflect the intensity of weathering but also indirectly indicate the degree of dryness and wetness of the palaeoclimate (Lv *et al.*, 2022). An increase in the CIA indicates a warmer and wetter climate (Nesbitt and Young, 1982), whereas increases in WIP and τ_{Na}

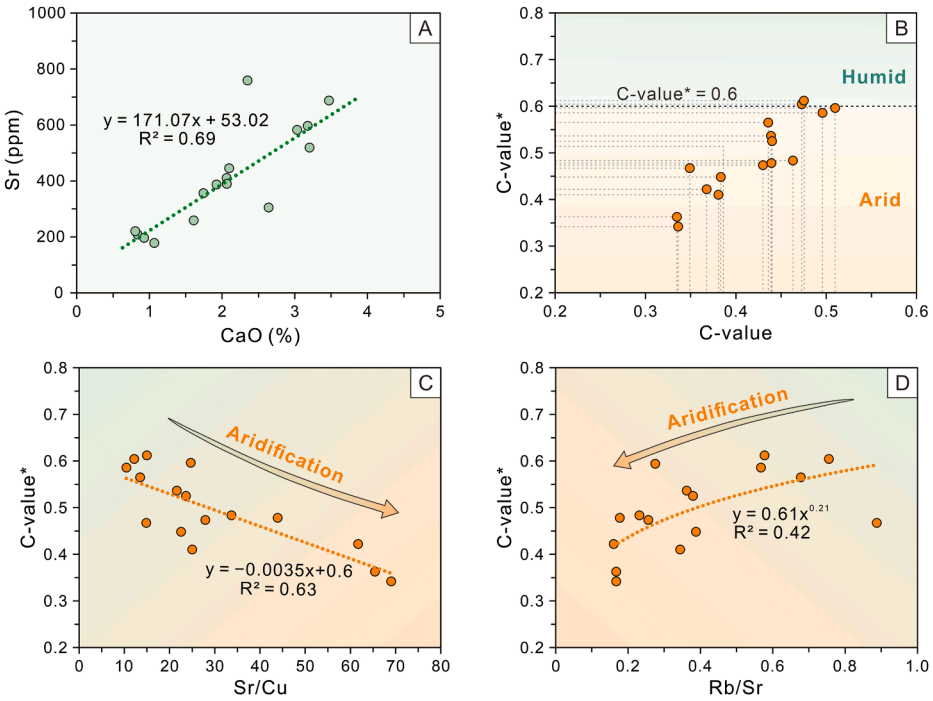

Fig. 14 Cross-plots of **A)** Sr versus CaO, **B)** C-value* versus C-value, **C)** C-value* versus Sr/Cu, and **D)** C-value* versus Rb/Sr for estimating the interference of carbonate-sourced elements on palaeoclimate proxies. See Supplementary Tables S3 and S4 for the source data.

indicate cooler and drier climates (Parker, 1970; Anderson *et al.*, 2002). This study indicates that all chemical weathering indices exhibit similar trends in weathering and climate fluctuations (Fig. 15A—E). After the interference of nonweathering factors such as diagenesis, provenance, sediment recycling, and sedimentary sorting on chemical weathering indices was systematically eliminated, the CIA and WIP were accurately corrected to the CIA* and WIP*. On this basis, LST has also been correspondingly revised to LST* by using the CIA* (Fig. 15C—E). This method of using the CIA* to estimate the LST after eliminating potassium metasomatism has been proven to be reliable by previous studies (Lv *et al.*, 2022; Zhang *et al.*, 2023b). LST and MAT, two proxies of palaeotemperature values, also exhibited extremely consistent fluctuations (Fig. 15C and D).

In modern sediments, sensitive element proxies such as Sr, Cu, and Rb have been widely applied to reconstruct palaeoclimates (Mathews *et al.*, 2020; Lv *et al.*, 2022). A Sr/Cu ratio of <10 reflects warm and humid climate conditions, and a value of over 10 indicates cold and arid conditions (Lerman *et al.*, 1995). A low Rb/Sr value represents a cool and arid climate, whereas a high Rb/Sr value reflects a warm and humid climate. An increase in the C-value indicates warmer and wetter climates, whereas a decrease in the C-value reflects colder and drier climates (Nesbitt and Young, 1982). Therefore, typically, the trends of the C-value and Rb/Sr ratio are opposite to those of Sr/Cu, whereas the trend of the Rb/Sr ratio is consistent with that of the C-value (Fig. 15F—H). This study confirms the synergistic evolution trend among these three climate proxies, and shows coupling variation with multiple chemical weathering indices (Fig. 15A—H).

The Early Cretaceous was characterized by a long-term greenhouse climate with high CO2 levels in the atmosphere (Cojan *et al.*, 2000; Wang *et al.*, 2014). However, an increasingly large body of evidence suggests that episodic global "cold snaps" punctuated the long-term greenhouse trend of the Early Cretaceous (Erba and Tremolada, 2004; Price and Passey, 2013; Vickers *et al.*, 2019). The Weissert Event (Valanginian cold snap) was the largest global climate cooling event of that period, lasting ~1.3 Ma (Cavalheiro *et al.*, 2021), and the latest research suggested that it may have been longer, lasting ~8.6 Ma (Vickers *et al.*, 2019). Furthermore, evidences of Aptian cooling events are proposed on the basis of sea surface temperature reconstructions (McAnena *et al.*, 2013: ~5 °C cooling), belemnite δ18O records (Bodin *et al.*, 2015: ~4 °C cooling), and worldwide-distributed diatomaceous earth (Vickers *et al.*, 2019: <7 °C). The sampling interval in this study corresponds mainly to the early Aptian (~120—118 Ma; Fig. 3). The

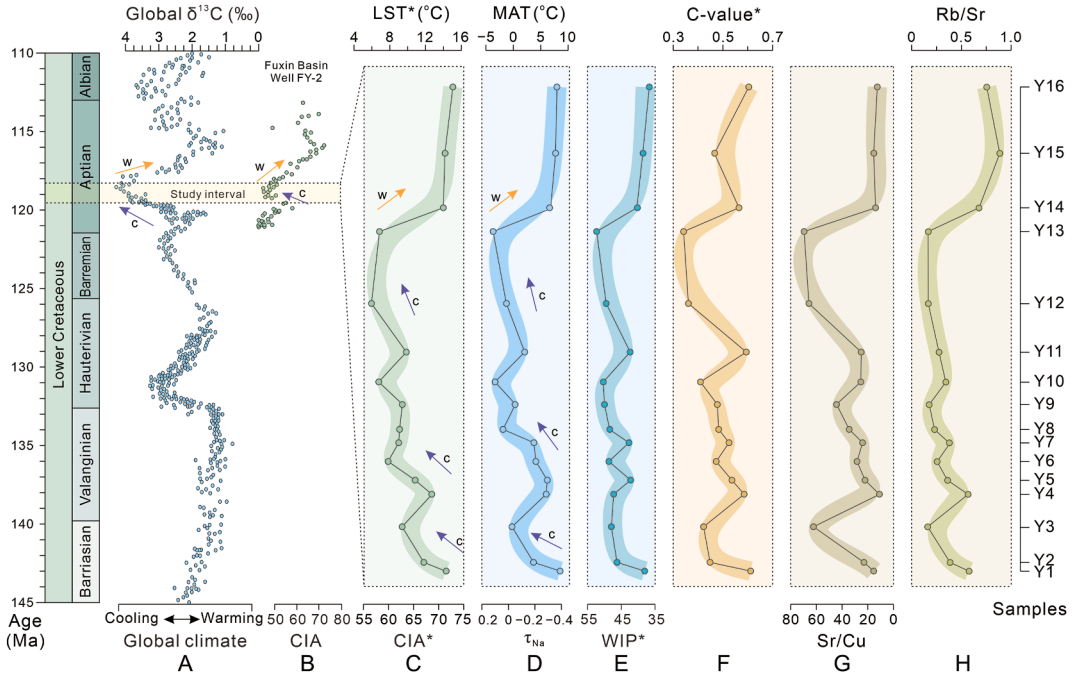

Fig. 15 **A)** Global age-calibrated $\delta^{13}C$ curve representing global temperature (constructed from Weissert and Erba, 2004); **B)** CIA index reconstruction results for Well FY-2 in the Fuxin Basin, northeastern China (modified from Jia *et al.*, 2023); **C—H)** Vertical variations in palaeoweathering indices, palaeoclimate proxies, and palaeotemperatures from the mudstone samples of the upper Xiguayuan Formation, Yuying section, Luanping Basin. c: cooling; w: warming. See Supplementary Tables S3 and S4 for the source data.

trends of all palaeoweathering indices and palaeoclimate proxies in the study interval are consistent with the global age-calibrated $\delta^{13}C$ curve (Fig. 15). The negative excursion of $\delta^{13}C$ usually indicates a warmer climate, whereas the positive excursion refers to a colder climate (Vickers *et al.*, 2019). Notably, the weathering intensity and climate conditions in the study interval are synchronized with global climate changes (Fig. 15A). Moreover, the CIA index in this study is similar to the index value of the Fuxin Basin reported by Jia *et al.* (2023), and the change trend is consistent (Fig. 15B and C).

Interestingly, volcanic activity can be observed in the strata that formed at approximately 120 ± 0.5 Ma in the study area (Wei *et al.*, 2012), which corresponds to the low values in the global age-calibrated $\delta^{13}C$ curve. There are two possible explanations for this phenomenon: first, the early Aptian climate cooling in the Luanping Basin was attributed to regional climate change, and it may be that the volcanic ash formed after a small-scale volcanic eruption blocked the reflection of the sun, thereby cooling the regional climate; second, regional climate change was controlled by global climate cooling. A series of studies support the occurrence of a large-scale volcanic eruption event at a global scale at approximately 120 Ma (Wei *et al.*, 2012; Pan *et al.*, 2021), which indicates that early Aptian global climate cooling can be attributed to volcanic activity derived from plate movement. Therefore, the terrestrial palaeoweathering and palaeoclimate of the Luanping Basin effectively record the early Aptian global climate cooling event.

6. Conclusions

1) The variation trends in multiple chemical weathering indices are reconstructed from the elemental geochemical compositions of the upper Xiguayuan Formation mudstones, Luanping Basin, indicating that the source area experienced mainly weak to moderate weathering intensity. On the basis of the Sr/Cu, Rb/Sr, and C-values, it can be concluded that the palaeoclimate conditions were arid and cold. The palaeotemperatures are quantitatively reconstructed, i.e., the range of the LST was 5.5 °C—12.6 °C, with an average of 9.0 °C, and the range of the MAT was −3.7 °C to 8.6 °C, with an average of 2.9 °C.
2) The potential interferences of diagenesis, provenance, sediment recycling, and sedimentary sorting were excluded by using the corresponding chemical proxies in the study interval. We confirmed the presence of K-metasomatism during the diagenesis process of the samples and eliminated its interference, restoring the original chemical weathering index. On the basis of the elimination of K-metasomatism, the correlation between the source composition and the corrected weathering index is weak, indicating that chemical weathering is not affected by interference from the source composition and its variations. The interference of sediment recycling and sedimentary sorting on weathering indices can also be disregarded.
3) The influence of carbonate-derived elements on palaeoclimate proxies was evaluated. Although the significant correlation between bulk Sr and CaO abundances indicates that a considerable proportion of Sr is derived from carbonates, carbonate-derived Sr is still investigated as a proxy for palaeoclimate dryness and wetness. Moreover, carbonate-derived Ca significantly interferes with C-values. After elimination, the correlation between the corrected C-value and the bimetallic proxies is significantly enhanced.
4) This study indicates that all chemical weathering indices and palaeoclimate proxies exhibit similar trends in weathering and climate fluctuations. The trends of all palaeoweathering indices and palaeoclimate proxies in the study interval are consistent with the global age-calibrated $\delta^{13}C$ curve, indicating that weathering intensity and climate conditions are synchronized with global climate change. Climate change at the regional and global scales may be closely related to volcanic activity caused by plate movement.

CRediT authorship contribution statement

Long Sun: Writing — original draft, Methodology. **Sheng-He Wu:** Supervision, Resources, Project administration, Funding acquisition. **Da-Li Yue:** Validation, Supervision, Funding acquisition. **Si-Chong Jiang:** Software, Investigation. **Wei Du:** Software. **Li-Jun Yang:** Software, Writing — review & editing. **Zhen-Hua Xu:** Validation. **Ke Zhang:** Investigation. All authors read and approved the final manuscript.

Availability of data and material

All data generated or analysed during this study are included in this published article and its supplementary information files.

Funding

This work was financially supported by the National Natural Science Foundation of China (Grant No. 42272110; 42272186).

Declaration of competing interest

The authors declare that they have no known competing financial interests or personal relationships that could have appeared to influence the work reported in this paper.

Acknowledgements

We are grateful to Professor Zeng-Zhao Feng, the founding editor-in-chief of the *Journal of Palaeogeography*, for his extensive guidance on research methods and writing skills during his lifetime. We also appreciate the constructive comments provided by the editors and reviewers, which greatly improved the quality of this article.

References

Anderson, S.P., Dietrich, W.E., Brimhall, G.H., 2002. Weathering profiles, mass-balance analysis, and rates of solute loss: Linkages between weathering and erosion in a small, steep catchment. *Geological Society of America Bulletin*, 114(9), 1143—1158. https://doi.org/10.1130/0016-7606(2002)114<1143:WPMBAA>2.0.CO;2.

Armstrong-Altrin, J.S., Lee, Y.I., Verma, S.P., Ramasamy, S., 2004. Geochemistry of sandstones from the upper Miocene Kudankulam Formation, southern India: Implications for provenance, weathering, and tectonic setting. *Journal of Sedimentary Research*, 74(2), 285—297. https://doi.org/10.1306/082803740285.

Bodin, S., Meissner, P., Janssen, N.M.M., Steuber, T., Mutterlose, J., 2015. Large igneous provinces and organic carbon burial: Controls on global temperature and continental weathering during the Early Cretaceous. *Global and Planetary Change*, 133, 238—253. https://doi.org/10.1016/j.gloplacha.2015.09.001.

Bomou, B., Adatte, T., Tantawy, A.A., Mort, H., Fleitmann, D., Huang, Y., F Llmi, K.B., 2013. The expression of the Cenomanian—Turonian oceanic anoxic event in Tibet. *Palaeogeography, Palaeoclimatology, Palaeoecology*, 369, 466—481. https://doi.org/10.1016/j.palaeo.2012.11.011.

Cai, Q.S., Hu, M.Y., Kane, O.I., Yang, Z., Wen, Y.R., Luo, Q., Li, M.T., Hu, Z.G., Deng, Q.J., 2023. Petrological and geochemical characteristics of the Ordovician—Silurian black shale in eastern Sichuan and western Hubei, South China: Differential sedimentary responses to tectonism and glaciation. *Journal of Palaeogeography*, 12(1), 129—152. https://doi.org/10.1016/j.jop.2022.09.003.

Cavalheiro, L., Wagner, T., Steinig, S., Bottini, C., Dummann, W., Esegbue, O., Gambacorta, G., Giraldo-Gómez, V., Farnsworth, A., Flögel, S., Hofmann, P., Lunt, D.J., Rethemeyer, J., Torricelli, S., Erba, E., 2021. Impact of global cooling on Early Cretaceous high pCO_2 world during the Weissert Event. *Nature Communications*, 12, 5411. https://doi.org/10.1038/s41467-021-25706-0.

Chamley, H., 1994. Clay mineral diagenesis. In: Parker, A., Sellwood, B.W. (Eds.), *Quantitative Diagenesis: Recent Developments and Applications to Reservoir Geology*. Springer, Dordrecht, pp. 161—188. https://doi.org/10.1007/978-94-011-0189-9_5.

Chen, D., Jiang, F.J., Pang, X.Q., Meng, L.J., Wang, Z.J., Xu, Z., Zhang, X., Huo, L.N., Wen, J.H., Zhao, R.J., Li, Y., 2023. Middle Eocene terrestrial paleoweathering and climate evolution in the midlatitude Bohai Bay Basin of eastern China. *Petroleum Science*, 20(3), 1471—1487. https://doi.org/10.1016/j.petsci.2022.12.013.

Chen, J., Wang, Y.J., Chen, Y., Liu, L.W., Ji, J.F., Lu, H.Y., 2000. Rb and Sr geochemical characterization of the Chinese loess stratigraphy and its implications for palaeomonsoon climate. *Acta Geologica Sinica (English Edition)*, 74(2), 279—288. https://doi.org/10.1111/j.1755-6724.2000.tb00462.x.

Chen, T., Zhang, J.L., Li, Y., Zhao, Y.F., 2021. Quantitative reconstruction of the palaeoclimate of the Shahejie Formation in the Chezhen Depression, Bohai Bay Basin, eastern China. *Frontiers of Earth Science*, 15(4), 909—921. https://doi.org/10.1007/s11707-021-0932-7.

Cojan, I., Moreau, M.G., Stott, L.E., 2000. Stable carbon isotope stratigraphy of the Paleogene pedogenic series of southern France as a basis for continental-marine correlation. *Geology*, 28(3), 259—262. https://doi.org/10.1130/0091-7613(2000)028<0259:SCISOT>2.3.CO;2.

Cope, T.D., Graham, S.A., 2007. *Upper crustal response to Mesozoic tectonism in western Liaoning, North China, and implications for lithospheric delamination*, vol. 280. Geological Society, London, Special Publications, pp. 201—222.

Cope, T., Luo, P., Zhang, X.Y., Zhang, X.J., Song, J.M., Zhou, G., Shultz, M.R., 2010. Structural controls on facies distribution in a small half-graben basin: Luanping basin, northeast China. *Basin Research*, 22(1), 33—44. https://doi.org/10.1111/j.1365-2117.2009.00417.x.

Cox, R., Lowe, D.R., Cullers, R.L., 1995. The influence of sediment recycling and basement composition on evolution of mudrock chemistry in the southwestern United States. *Geochimica et Cosmochimica Acta*, 59(14), 2919—2940. https://doi.org/10.1016/0016-7037(95)00185-9.

Davis, G.A., Zheng, Y.D., Wang, C., Darby, B.J., Zhang, C.H., Gehrels, G., 2001. Mesozoic tectonic evolution of the Yanshan fold and thrust belt, with emphasis on

Hebei and Liaoning provinces, northern China. In: Hendrix, M.S., Davis, G.A. (Eds.), *Paleozoic and Mesozoic Tectonic Evolution of Central and Eastern Asia: From Continental Assembly to Intracontinental Deformation. Geological Society of America Memoirs*, vol. 194, pp. 171—197. https://doi.org/10.1130/0-8137-1194-0.171.

Dinis, P., Garzanti, E., Vermeesch, P., Huvi, J., 2017. Climatic zonation and weathering control on sediment composition (Angola). *Chemical Geology*, 467, 110—121. https://doi.org/10.1016/j.chemgeo.2017.07.030.

Erba, E., Tremolada, F., 2004. Nannofossil carbonate fluxes during the Early Cretaceous: Phytoplankton response to nutrification episodes, atmospheric CO2, and anoxia. *Paleoceanography*, 19(1), PA1008. https://doi.org/10.1029/2003PA000884.

Fang, Y.N., Olsen, P., Zheng, D.R., Xue, N.H., Wang, H., Xu, C.P., Li, S., Wang, B., Zhang, H.C., 2022. A new astronomical time scale for the early Jehol Biota in the Luanping Basin, northeastern China. *Palaeogeography, Palaeoclimatology, Palaeoecology*, 607, 111273. https://doi.org/10.1016/j.palaeo.2022.111273.

Fedo, C.M., Nesbitt, H.W., Young, G.M., 1995. Unraveling the effects of potassium metasomatism in sedimentary-rocks and paleosols, with implications for paleoweathering conditions and provenance. *Geology*, 23(10), 921—924. https://doi.org/10.1130/0091-7613(1995)023<0921:UTEOPM>2.3.CO;2.

Gao, S., Luo, T.C., Zhang, B.R., Zhang, H.F., Han, Y.W., Zhao, Z.D., Hu, Y.K., 1998. Chemical composition of the continental crust as revealed by studies in East China. *Geochimica et Cosmochimica Acta*, 62(11), 1959—1975. https://doi.org/10.1016/S0016-7037(98)00121-5.

Garzanti, E., Padoan, M., Setti, M., López-Galindo, A., Villa, I.M., 2014. Provenance versus weathering control on the composition of tropical river mud (southern Africa). *Chemical Geology*, 366, 61—74. https://doi.org/10.1016/j.chemgeo.2013.12.016.

Haq, B.U., Hardenbol, J., Vail, P.R., 1987. Chronology of fluctuating sea level since Triassic (250 million years ago to present). *Science*, 235, 1156—1167.

Harland, M., Francis, J.E., Brentnall, S.J., Beerling, D.J., 2007. Cretaceous (Albian—Aptian) conifer wood from Northern Hemisphere high latitudes: Forest composition and palaeoclimate. *Review of Palaeobotany and Palynology*, 143(3), 167—196. https://doi.org/10.1016/j.revpalbo.2006.07.005.

Harnois, L., 1988. The CIW index: A new chemical index of weathering. *Sedimentary Geology*, 55(3—4), 319—322. https://doi.org/10.1016/0037-0738(88)90137-6.

Hu, Y., Hu, J., Du, Y.B., Lu, H.N., Yang, N., Wang, L., Xu, H. H., 2023. Early Cretaceous palynofloras from the Bongor Basin, Chad, and their palaeoenvironmental and palaeoclimatic significances. *Journal of African Earth Sciences*, 198, 104792. https://doi.org/10.1016/j.jafrearsci.2022.104792.

Huber, B.T., Norris, R.D., MacLeod, K.G., 2002. Deep-sea paleotemperature record of extreme warmth during the Cretaceous. *Geology*, 30(2), 123—126. https://doi.org/10.1130/0091-7613(2002)030<0123:DSPROE>2.0.CO;2.

Jia, J.L., Miao, C.S., Xie, W.Q., 2023. Terrestrial paleoclimate transition associated with continental weathering and drift during the Aptian—Albian of East Asia. *Geological Society of America Bulletin*, 135(1—2), 467—480. https://doi.org/10.1130/B36253.1.

Lerman, A., Imboden, D.M., Gat, J.R., Chou, L., 1995. *Physics and Chemistry of Lakes*, second ed. Springer-Verlag, Heidelberg.

Li, C., Yang, S.Y., 2010. Is chemical index of alteration (CIA) a reliable proxy for chemical weathering in global drainage basins? *American Journal of Science*, 310(2), 111—127.

Li, Y., 2003. Fan-deltaic depositional systems of the Xiguayuan Formation in Luanping Basin. *Acta Geoscientica Sinica*, 24(4), 353—356. https://doi.org/10.3321/j.issn:1006-3021.2003.04.011 (in Chinese with English abstract).

Liu, B., Song, Y., Zhu, K., Su, P., Ye, X., Zhao, W.C., 2020. Mineralogy and element geochemistry of salinized lacustrine organic-rich shale in the Middle Permian Santanghu Basin: Implications for paleoenvironment, provenance, tectonic setting and shale oil potential. *Marine and Petroleum Geology*, 120, 104569. https://doi.org/10.1016/j.marpetgeo.2020.104569.

Liu, G., Zhou, D.S., 2007. Application of microelements analysis in identifying sedimentary environment—Taking Qianjiang Formation in the Jianghan Basin as an example. *Petroleum Geology and Experiment*, 29(3), 307—310. https://doi.org/10.3969/j.issn.1001-6112.2007.03.016 (in Chinese with English abstract).

Lv, D.W., Du, W.X., Zhang, Z.H., Gao, Y., Wang, T.T., Xu, J. C., Zhang, A.C., Wang, C.S., 2024. A synthesis of the Cretaceous wildfire record related to atmospheric oxygen levels? *Journal of Palaeogeography*, 13(1), 149—164. https://doi.org/10.1016/j.jop.2023.10.001.

Lv, D.W., Wang, L.J., Isbell, J.L., Lu, C.Y., Li, P.P., Wang, Y. J., Zhang, Z.H., 2022. Records of chemical weathering and volcanism linked to paleoclimate transition during the Late Paleozoic Icehouse. *Global and Planetary Change*, 217, 103934. https://doi.org/10.1016/j.gloplacha.2022.103934.

Ma, Y., Yang, H.Z., Ma, Y.Y., Wang, Y.P., Wu, W.Z., An, N., Tian, S.F., Ma, L., Fu, D.L., 2023. Geochemical characteristics of shales from Upper Carboniferous Yanghugou formation in Weiningbeishan area, China: Implication for provenance, source weathering and tectonic setting. *Marine and Petroleum Geology*, 149, 106082. https://doi.org/10.1016/j.marpetgeo.2022.106082.

Mathews, R.P., Pillai, S.S.K., Manoj, M.C., Agrawal, S., 2020. Palaeoenvironmental reconstruction and evidence of marine influence in Permian coal-bearing sequence from Lalmatia Coal mine (Rajmahal Basin), Jharkhand, India: A multi-proxy approach. *International Journal of Coal Geology*, 224, 103485. https://doi.org/10.1016/j.coal.2020.103485.

McAnena, A., Flögel, S., Hofmann, P., Herrle, J.O., Griesand, A., Pross, J., Talbot, H.M., Rethemeyer, J., Wallmann, K., Wagner, T., 2013. Atlantic cooling associated with a marine biotic crisis during the mid-

Cretaceous period. *Nature Geoscience*, 6(7), 558—561. https://doi.org/10.1038/ngeo1850.

McLennan, S.M., 1993. Weathering and global denudation. *The Journal of Geology*, 101(2), 295—303.

Menzies, M., Xu, Y.G., Zhang, H.F., Fan, W.M., 2007. Integration of geology, geophysics and geochemistry: A key to understanding the North China Craton. *Lithos*, 96 (1—2), 1—21. https://doi.org/10.1016/j.lithos.2006.09.008.

Moosavirad, S.M., Janardhana, M.R., Sethumadhav, M.S., Moghadam, M.R., Shankara, M., 2011. Geochemistry of Lower Jurassic shales of the Shemshak Formation, Kerman Province, Central Iran: Provenance, source weathering and tectonic setting. *Chemie der Erde - Geochemistry*, 71(3), 279—288. https://doi.org/10.1016/j.chemer.2010.10.001.

Nesbitt, H.W., Young, G.M., 1982. Early Proterozoic climates and plate motions inferred from major element chemistry of lutites. *Nature*, 299(5885), 715—717. https://doi.org/10.1038/299715a0.

Nesbitt, H.W., Young, G.M., 1989. Formation and diagenesis of weathering profiles. *The Journal of Geology*, 97(2), 129—147. https://doi.org/10.1086/629290.

Pan, S.B., Jiang, Z.X., Zhang, Y.F., Yuan, X.D., Liao, Y.H., 2021. Geochemical characteristics of the Lower Cretaceous Xiguayuan Formation mudrocks in the Luanping Basin, northern China: Implications for the hydrocarbon generation potential and sedimentary environments. *Marine and Petroleum Geology*, 133, 105256. https://doi.org/10.1016/j.marpetgeo.2021.105256.

Panahi, A., Young, G.M., Rainbird, R.H., 2000. Behavior of major and trace elements (including REE) during Paleoproterozoic pedogenesis and diagenetic alteration of an Archean granite near Ville Marie, Québec, Canada. *Geochimica et Cosmochimica Acta*, 64(13), 2199—2220. https://doi.org/10.1016/S0016-7037(99)00420-2.

Parker, A., 1970. An index of weathering for silicate rocks. *Geological Magazine*, 107(6), 501—504.

Price, G.D., Passey, B.H., 2013. Dynamic polar climates in a greenhouse world: Evidence from clumped isotope thermometry of Early Cretaceous belemnites. *Geology*, 41 (8), 923—926. https://doi.org/10.1130/G34484.1.

Qadrouh, A.N., Alajmi, M.S., Alotaibi, A.M., Baioumy, H., Almalki, M.A., Alyousif, M.M., Ahmed Salim, A.M., Bin Rogaib, A.M., 2021. Mineralogical and geochemical imprints to determine the provenance, depositional environment, and tectonic setting of the Early Silurian source rock of the Qusaiba shale, Saudi Arabia. *Marine and Petroleum Geology*, 130, 105131. https://doi.org/10.1016/j.marpetgeo.2021.105131.

Qi, L., Cawood, P.A., Yang, J.H., Xu, Y.J., Du, Y.S., 2020. Quantifying temperature variation between Neoproterozoic cryochron—nonglacial interlude, Nanhua Basin, South China. *Precambrian Research*, 351, 105967. https://doi.org/10.1016/j.precamres.2020.105967.

Qian, S.P., Ren, Z.Y., Richard, W., Zhang, L., Zhang, Y.H., Hong, L.B., Ding, X.L., Wu, Y.D., 2017. Petrogenesis of Early Cretaceous basaltic lavas from the North China Craton: Implications for cratonic destruction. *Journal of Geophysical Research: Solid Earth*, 122(3), 1900—1918. https://doi.org/10.1002/2016JB013548.

Qiao, D.W., Peng, N., Kuang, H.W., Liu, Y.Q., Liu, Y.X., Cui, L.W., Wang, Y.C., 2022. Changes in prevailing surface-paleowinds reveal the atmospheric circulation transition during Early Cretaceous in North China. *Palaeogeography, Palaeoclimatology, Palaeoecology*, 586, 110784. https://doi.org/10.1016/j.palaeo.2021.110784.

Rasmussen, C., Brantley, S., Richter, D. deB., Blum, A., Dixon, J., White, A.F., 2011. Strong climate and tectonic control on plagioclase weathering in granitic terrain. *Earth and Planetary Science Letters*, 301(3—4), 521—530. https://doi.org/10.1016/j.epsl.2010.11.037.

Rieu, R., Allen, P.A., Plotze, M., Pettke, T., 2007. Compositional and mineralogical variations in a Neoproterozoic glacially influenced succession, Mirbat area, south Oman: Implications for paleoweathering conditions. *Precambrian Research*, 154(3—4), 248—265. https://doi.org/10.1016/j.precamres.2007.01.003.

Roddaz, M., Viers, J.M., Brusset, S., Baby, P., Boucayrand, C., Hérail, G., 2006. Controls on weathering and provenance in the Amazonian foreland basin: Insights from major and trace element geochemistry of Neogene Amazonian sediments. *Chemical Geology*, 226 (1—2), 31—65. https://doi.org/10.1016/j.chemgeo.2005.08.010.

Roddaz, M., Viers, J.M., Brusset, S., Baby, P., Hérail, G., 2005. Sediment provenances and drainage evolution of the Neogene Amazonian foreland basin. *Earth and Planetary Science Letters*, 239(1—2), 57—78. https://doi.org/10.1016/j.epsl.2005.08.007.

Scotese, C.R., 2021. An atlas of Phanerozoic paleogeographic maps: The seas come in and the seas go out. *Annual Review of Earth and Planetary Sciences*, 49, 679—728. https://doi.org/10.1146/annurev-earth-081320-064052.

Sheldon, N.D., Tabor, N.J., 2009. Quantitative paleoenvironmental and paleoclimatic reconstruction using paleosols. *Earth-Science Reviews*, 95(1—2), 1—52. https://doi.org/10.1016/j.earscirev.2009.03.004.

Sun, F.N., Hu, W.X., Cao, J., Wang, X.L., Zhang, Z.R., Ramezani, J., Shen, S.Z., 2022b. Sustained and intensified lacustrine methane cycling during Early Permian climate warming. *Nature Communications*, 13, 4856. https://doi.org/10.1038/s41467-022-32438-2.

Sun, L., Wu, S.H., Yue, D.L., Cui, W.F., 2024b. Paleosalinity reconstruction in offshore lacustrine basins based on elemental geochemistry: a case study of Middle-Upper Eocene Shahejie Formation, Zhanhua Sag, Bohai Bay Basin. *Journal of Oceanology and Limnology*, 42(4), 1087—1105.

Sun, L., Wu, S.H., Yue, D.L., Jiang, S.C., Xiao, K., Li, X.B., Huang, Q.Z., Xu, Z.H., Xiong, Q.C., 2024a. Mineralogical and geochemical characteristics of mudstones from the Lower Cretaceous Prosopis Formation in the Bongor basin, Chad: Implications for provenance, paleoenvironment and organic matter enrichment. *Marine and Petroleum Geology*, 168, 107031. https://doi.org/10.1016/j.marpetgeo.2024.107031.

Sun, L., Zhang, J.L., Li, Y., Yan, X., Zhang, X.C., 2022c. Paleosalinity and lake level fluctuations of the 3rd Member of Paleogene Shahejie Formation, Chezhen Sag, Bohai Bay Basin. *Frontiers of Earth Science*, 16(4), 949—962.

Sun, L., Zhang, J.L., Zhang, T.Y., Yan, X., Chen, T., Liu, J.S., 2022a. Paleosalinity reconstruction for the Paleocene sequence of Lishui Sag in the East China Sea Shelf Basin. *Arabian Journal for Science and Engineering*, 47 (6), 7433—7448. https://doi.org/10.1007/s13369-022-06696-7.

Tan, M.X., Zhu, X.M., Geng, M.Y., Zhu, S.F., Liu, W., 2017. The occurrence and transformation of lacustrine sediment gravity flow related to depositional variation and paleoclimate in the Lower Cretaceous Prosopis Formation of the Bongor Basin, Chad. *Journal of African Earth Sciences*, 134, 134—148. https://doi.org/10.1016/j.jafrearsci.2017.06.003.

Tao, S., Xu, Y.B., Tang, D.Z., Xu, H., Li, S., Chen, S.D., Liu, W.B., Cui, Y., Gou, M.F., 2017. Geochemistry of the Shitoumei oil shale in the Santanghu Basin, Northwest China: Implications for paleoclimate conditions, weathering, provenance and tectonic setting. *International Journal of Coal Geology*, 184, 42—56. https://doi.org/10.1016/j.coal.2017.11.007.

Tarduno, J.A., Brinkman, D.B., Renne, P.R., Cottrell, R.D., Scher, H., Castillo, P., 1998. Evidence for extreme climatic warmth from Late Cretaceous Arctic vertebrates. *Science*, 282(5397), 2241—2243. https://doi.org/10.1126/science.282.5397.2241.

Taylor, S.R., McLennan, S.M., 1985. *The Continental Crust: Its Composition and Evolution*. Oxford, Blackwell, pp. 57—72.

Vickers, M.L., Price, G.D., Jerrett, R.M., Sutton, P., Watkinson, M.P., FitzPatrick, M.E.J., 2019. The duration and magnitude of Cretaceous cool events: Evidence from the northern high latitudes. *Geological Society of America Bulletin*, 131(11—12), 1979—1994. https://doi.org/10.1130/B35074.1.

Wang, Y.D., Huang, C.M., Sun, B.N., Quan, C., Wu, J.Y., Lin, Z.C., 2014. Paleo-CO2 variation trends and the Cretaceous greenhouse climate. *Earth-Science Reviews*, 129, 136—147. https://doi.org/10.1016/j.earscirev.2013.11.001.

Wei, H.H., Meng, Q.R., Wu, G.L., Li, L., 2012. Multiple controls on rift basin sedimentation in volcanic settings: Insights from the anatomy of a small Early Cretaceous basin in the Yanshan Belt, northern North China. *Geological Society of America Bulletin*, 124(3—4), 380—399. https://doi.org/10.1130/B30495.1.

Wei, W., Algeo, T.J., 2020. Elemental proxies for paleosalinity analysis of ancient shales and mudrocks. *Geochimica et Cosmochimica Acta*, 287, 341—366. https://doi.org/10.1016/j.gca.2019.06.034.

Weissert, H., Erba, E., 2004. Volcanism, CO2 and palaeoclimate: A Late Jurassic—Early Cretaceous carbon and oxygen isotope record. *Journal of the Geological Society*, 161(4), 695—702. https://doi.org/10.1144/0016-764903-087.

Wu, F.D., Chen, Y.J., Li, Y., Jiao, Y.Q., 2000. Tectonic evolutions and their control on development of fan-deltic depositional system in the Luanping Basin. *Geoscience*, 14(2), 179—184. https://doi.org/10.3969/j.issn.1000-8527.2000.02.010 (in Chinese with English abstract).

Yamamoto, K., Sugisaki, R., Arai, F., 1986. Chemical aspects of alteration of acidic tuffs and their application to siliceous deposits. *Chemical Geology*, 55(1—2), 61—76. https://doi.org/10.1016/0009-2541(86)90128-2.

Yan, D.Z., Xu, H.M., Xu, Z.H., Lei, Z.C., Tian, M., Cheng, L., Ma, Y.H., Wang, Z.L., Ostadhassan, M., 2020. Sedimentary architecture of hyperpycnal flow deposits: Cretaceous Sangyuan outcrop, from the Luanping Basin, North East China. *Marine and Petroleum Geology*, 121, 104593. https://doi.org/10.1016/j.marpetgeo.2020.104593.

Yang, J.H., Cawood, P.A., Du, Y.S., Condon, D.J., Yan, J.X., Liu, J.Z., Huang, Y., Yuan, D.X., 2018. Early Wuchiapingian cooling linked to Emeishan basaltic weathering? *Earth and Planetary Science Letters*, 492, 102—111. https://doi.org/10.1016/j.epsl.2018.04.004.

Yang, J.H., Cawood, P.A., Du, Y.S., Feng, B., Yan, J.X., 2014. Global continental weathering trends across the Early Permian glacial to postglacial transition: Correlating high- and low-paleolatitude sedimentary records. *Geology*, 42(10), 835—838.

Yang, J.H., Cawood, P.A., Du, Y.S., Li, W.Q., Yan, J.X., 2016a. Reconstructing Early Permian tropical climates from chemical weathering indices. *GSA Bulletin*, 128 (5—6), 739—751. https://doi.org/10.1130/B31371.1.

Yang, J.H., Cawood, P.A., Montañez, I.P., Condon, D.J., Du, Y.S., Yan, J.X., Yan, S.Q., Yuan, D.X., 2020. Enhanced continental weathering and large igneous province induced climate warming at the Permo-Carboniferous transition. *Earth and Planetary Science Letters*, 534, 116074. https://doi.org/10.1016/j.epsl.2020.116074.

Yang, J.H., Du, Y.S., 2017. Weathering geochemistry and palaeoclimate implication of the Early Permian mudstones from eastern Henan Province, North China. *Journal of Palaeogeography*, 6(4), 370—380. https://doi.org/10.1016/j.jop.2017.08.003.

Yang, Y.B., Fang, X.M., Galy, A., Jin, Z.D., Wu, F.L., Yang, R. S., Zhang, W.L., Zan, J.B., Liu, X.M., Gao, S.P., 2016b. Plateau uplift forcing climate change around 8.6 Ma on the northeastern Tibetan Plateau: Evidence from an integrated sedimentary Sr record. *Palaeogeography, Palaeoclimatology, Palaeoecology*, 461, 418—431. https://doi.org/10.1016/j.palaeo.2016.09.002.

Yang, Y.B., Fang, X.M., Koutsodendris, A., Ye, C.C., Yang, R. S., Zhang, W.L., Liu, X.M., Gao, S.P., 2016c. Exploring Quaternary paleolake evolution and climate change in the western Qaidam Basin based on the bulk carbonate geochemistry of lake sediments. *Palaeogeography, Palaeoclimatology, Palaeoecology*, 446, 152—161. https://doi.org/10.1016/j.palaeo.2016.01.021.

Ye, C.C., Yang, Y.B., Fang, X.M., Zhang, W.L., 2016. Late Eocene clay boron-derived paleosalinity in the Qaidam Basin and its implications for regional tectonics and climate. *Sedimentary Geology*, 346, 49—59. https://doi.org/10.1016/j.sedgeo.2016.10.006.

Zhang, K., Wu, S.H., Wang, H.H., Mi, Z.R., Qu, J.H., Wang, Z.K., Wang, H.N., 2023a. Sedimentary architecture of shallow-water fan-delta front in a lacustrine basin: Sangyuan section of Lower Cretaceous Xiguayuan Formation, Luanping Basin, northeast China. *Swiss Journal of Geosciences*, 116, 3. https://doi.org/10.1186/s00015-023-00432-5.

Zhang, S.H., Zhao, Y., Davis, G.A., Ye, H., Wu, F., 2014. Temporal and spatial variations of Mesozoic magmatism

and deformation in the North China Craton: Implications for lithospheric thinning and decratonization. *Earth-Science Reviews*, 131, 49—87. https://doi.org/10.1016/j.earscirev.2013.12.004.

Zhang, Y.F., Yuan, X.D., Wang, M., Ge, P.C., Huo, Y.C., Xu, J., Zhang, J.G., Cheng, J., Jiang, Z.X., 2021. Discovery of lacustrine shale deposits in the Yanshan Orogenic Belt, China: Implications for hydrocarbon exploration. *Geoscience Frontiers*, 12(6), 101256. https://doi.org/10.1016/j.gsf.2021.101256.

Zhang, Z.H., Lv, D.W., Lu, M., Yu, Z.C., Gao, Y., Wang, T.T., Gao, J., Wang, C.S., 2023b. Wildfire activity driven by the 405-kyr orbital climate cycles in the Middle Jurassic. *Global and Planetary Change*, 222, 104069. https://doi.org/10.1016/j.gloplacha.2023.104069.

Zhao, Z.Y., Zhao, J.H., Wang, H.J., Liao, J.D., Liu, C.M., 2007. Distribution characteristics and applications of trace elements in Junggar Basin. *Natural Gas Exploration and Development*, 30(2), 30—32. https://doi.org/10.3969/j.issn.1673-3177.2007.02.007 (in Chinese with English abstract).

Supplementary data

Supplementary Tables S1—S5 to this article can be found online at https://doi.org/10.1016/j.jop.2025.100295.

Supplementary Table S1 Mineral compositions from the XRD results.

Supplementary Table S2 Clay mineral compositions from the XRD results.

Supplementary Table S3 Major element contents.

Supplementary Table S4 Trace element contents.

Supplementary Table S5 REE contents.